




Article

A Method for Predicting High-Resolution 3D Variations in Temperature and Salinity Fields Using Multi-Source Ocean Data

Xiaohu Cao ¹, Chang Liu ^{1,2}, Shaoqing Zhang ^{1,3,4} and Feng Gao ^{1,5,*}

¹ College of Intelligent Systems Science and Engineering, Harbin Engineering University, Harbin 150001, China; hycxh@hrbeu.edu.cn (X.C.); liuchang407@hrbeu.edu.cn (C.L.); szhang@ouc.edu.cn (S.Z.)

² Qingdao Hatran Ocean Intelligence Technology Co., Ltd., Qingdao 266400, China

³ Key Laboratory of Physical Oceanography, MOE, Institute for Advanced Ocean Study, Frontiers Science Center for Deep Ocean Multispheres and Earth System (DOMES), Ocean University of China, Qingdao 266100, China

⁴ The College of Ocean and Atmosphere, Ocean University of China, Qingdao 266100, China

⁵ Innovation and Development Center, Harbin Engineering University, Qingdao 266400, China

* Correspondence: gaofeng19@hrbeu.edu.cn

Abstract: High-resolution three-dimensional (3D) variations in ocean temperature and salinity fields are of great significance for ocean environment monitoring. Currently, AI-based 3D temperature and salinity field predictions rely on expensive 3D data, and as the prediction period increases, the stacking of high-resolution 3D data greatly increases the difficulty of model training. This paper transforms the prediction of 3D temperature and salinity into the prediction of sea surface elements and the inversion of subsurface temperature and salinity using sea surface elements, by leveraging the relationship between sea surface factors and subsurface temperature and salinity. This method comprehensively utilizes multi-source ocean data to avoid the issue of data volume caused by stacking high-resolution historical data. Specifically, the model first utilizes 1/4° low-resolution satellite remote sensing data to construct prediction models for sea surface temperature (SST) and sea level anomaly (SLA), and then uses 1/12° high-resolution temperature and salinity data as labels to build an inversion model of subsurface temperature and salinity based on SST and SLA. The prediction model and inversion model are integrated to obtain the final high-resolution 3D temperature and salinity prediction model. Experimental results show that the 20-day prediction results in the two sea areas of the coastal waters of China and the Northwest Pacific show good performance, accurately predicting ocean temperature and salinity in the vast majority of layers, and demonstrate higher resource utilization efficiency.

Keywords: 3D temperature and salinity fields; satellite remote sensing data; high-resolution temperature and salinity data; resource utilization efficiency



Citation: Cao, X.; Liu, C.; Zhang, S.; Gao, F. A Method for Predicting High-Resolution 3D Variations in Temperature and Salinity Fields Using Multi-Source Ocean Data. *J. Mar. Sci. Eng.* **2024**, *12*, 1396. <https://doi.org/10.3390/jmse12081396>

Academic Editor: Eugen Rusu

Received: 9 July 2024

Revised: 3 August 2024

Accepted: 12 August 2024

Published: 14 August 2024



Copyright: © 2024 by the authors. Licensee MDPI, Basel, Switzerland. This article is an open access article distributed under the terms and conditions of the Creative Commons Attribution (CC BY) license (<https://creativecommons.org/licenses/by/4.0/>).

1. Introduction

High-resolution three-dimensional (3D) temperature and salinity fields provide refined and comprehensive data support and analysis for marine environmental monitoring [1–5]. Accurately predicting changes in the 3D ocean temperature and salinity fields is of great significance. Currently, there are two main methods for 3D temperature and salinity prediction. The first method is based on physical dynamics using numerical models [6–8], which simulate ocean movement processes through a series of complex dynamic equations. However, this approach requires discretization of the complex dynamic equations, and the iterative process consumes a significant amount of computational resources.

The second method is based on data-driven deep learning prediction, which predicts by learning the patterns of data changes. Compared with traditional numerical models, deep learning methods have significant advantages in terms of computational cost and flexibility and have been widely applied in the field of ocean temperature and salinity

in recent years. For example, in temperature prediction, Zhang et al. [9] used the FC-LSTM model to estimate the time series of single-point SST, achieving higher accuracy than traditional SVM algorithms. However, single-point prediction models lack spatial correlation, and subsequent research [10–15] has improved algorithm models to further optimize the performance of sea temperature prediction algorithms.

In addition to improving model accuracy, combining physical methods has shown significant effects. For instance, Hou et al. [16] incorporated shortwave and longwave radiation into the prediction model, leveraging the physical relationship between SST and radiation to enhance SST prediction accuracy. Hu et al. [17] used deep learning algorithms to extract multi-variable physical features of the sea surface, improving the prediction accuracy of SST and other sea surface elements. Wu et al. [18] adopted a physics-guided deep learning algorithm to further enhance sea temperature prediction accuracy and improve the model's physical consistency.

In terms of salinity, Zhang et al. [19] used DNN neural networks to retrieve sea surface salinity, demonstrating the model's reliable performance in salinity learning. Liu et al. [20] proposed a neural network called DSE-NN, which effectively captures the spatiotemporal distribution characteristics and physical laws of salinity, achieving higher salinity reconstruction accuracy. Additionally, numerous studies [21–25] have shown that data-driven deep learning models can effectively learn the complex nonlinear relationships between input variables and salinity, resulting in more accurate salinity predictions.

Current research on ocean temperature and salinity prediction primarily focuses on the two-dimensional surface plane. However, for marine environmental monitoring, effective prediction in three-dimensional space is of greater significance. In recent years, Liu et al. [26] utilized TD-LSTM to predict the average seawater temperature at different depths for each observation point one month ahead. Zhang et al. [27] employed M-ConvLSTM to predict the 3D ocean temperature field. Due to the influence of thermoclines, which reduced prediction accuracy, Zuo et al. [28] proposed the SST-4D-CNN model to predict ocean temperature. Sun et al. [29] used the 3D-UNet model to predict SSbT above 400 m in the Pacific and its adjacent oceans. These methods require expensive 3D ocean data and have limitations in terms of temporal or spatial resolution of the predicted data. However, oceanic small-scale data play a critical role in detailed observations [30–32]. The current challenge in research is how to leverage existing ocean data to predict refined temperature and salinity information accurately.

Since many measurable sea surface elements can reflect internal oceanic changes, key internal ocean parameters can be inferred from them [33]. For example, Wu et al. [34] found that internal ocean dynamics, influenced by thermal expansion, can affect the sea surface, and SST can indirectly reflect changes in subsurface temperatures. Syst, E. [35] discovered that thermohaline expansion significantly contributes to sea level rise, which is closely related to ocean temperature. Based on this relationship, subsequent researchers [36–40] utilized sea surface elements to construct deep learning networks to invert subsurface temperature and salinity fields. The experimental results show that sea surface elements can effectively reconstruct 3D temperature and salinity fields.

The method proposed in this paper relies on the nonlinear relationship between SST, SLA, and subsurface 3D temperature and salinity fields, transforming 3D temperature and salinity prediction into horizontal sea surface element prediction and vertical sea surface to subsurface temperature and salinity inversion. The experimental steps are as follows: first, a $1/4^\circ$ low-resolution satellite remote sensing data-based M-ViT model is used for SST and SLA prediction. The prediction results are then temporally and spatially matched with reanalysis data, and the SimVP-gsta model is used to invert the subsurface 3D temperature and salinity fields, thereby achieving a $1/12^\circ$ high-resolution 3D temperature and salinity prediction model. Experimental results show that the proposed method can effectively predict changes in the subsurface 3D temperature and salinity fields within 20 days.

The rest of this paper is organized as follows: Section 2 will introduce the data used in the experiments, the research area, and the data partitioning methods. Section 3 will

provide a detailed description of the model components selected for this study. Section 4 will cover the experimental parameters and the evaluation metrics used. Section 5 will validate the effectiveness of the three-dimensional forecasting model constructed in this study. Section 6 will discuss the experimental results, and finally, Section 7 will present the conclusions of the study.

2. Dataset

The selected research areas for this study are the Coastal Waters of China (CWOC, 0° N–42° N, 105° E–130° E) and the Northwest Pacific Ocean (NWP, 10° S–42° N, 99° E–180° E). The sea surface forecast data used in this study come from NOAA’s OISST data (<https://www.ncei.noaa.gov/data>, accessed on 10 October 2023) and daily mean SLA data provided by CMEMS (<https://data.marine.copernicus.eu/products>, accessed on 10 October 2023), both with a resolution of 1/4°.

For the three-dimensional temperature and salinity inversion, the input data consist of OISST data interpolated using bilinear interpolation to match the spatial resolution of low-resolution satellite data and reanalysis data. The target data are high-precision reanalysis data provided by CMEMS (<https://data.marine.copernicus.eu/products>, accessed on 15 October 2023), with a resolution of 1/12° and comprising 50 layers. For the experiment, layers 1–48 are used as the target dataset for inversion, with each layer representing depth as detailed in Table 1.

For this forecasting and inversion experiment, data from 2006 to 2017 were selected as the training set, and data from 2018 to 2020 were used as the validation set. Data from December 2021 to November 2022, approximately one year, were used as the test set, and test results were statistically analyzed on a quarterly basis. The details of the training data partitioning are shown in the figure: Figure 1a shows the partitioning of the sea surface element prediction data, and Figure 1b shows the partitioning of the sea surface element inversion subsurface temperature and salinity data.

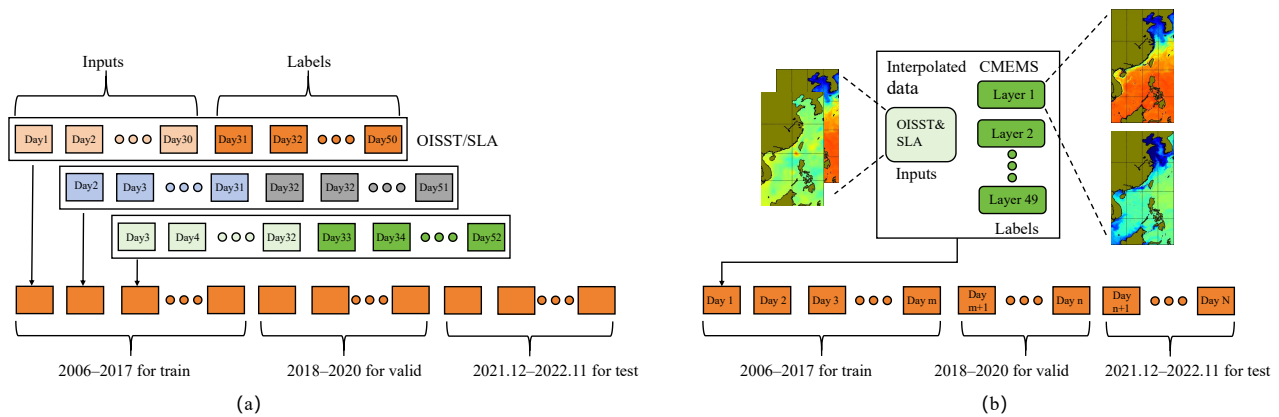


Figure 1. Data partitioning for prediction and inversion. Figure (a) shows the division of forecast data, and figure (b) shows the division of inversion data.

Table 1. Table of depth statistics for each layer of reanalysis data.

Layer	Depth	Layer	Depth	Layer	Depth	Layer	Depth
1	1 m	13	25 m	25	185 m	37	1452 m
2	2 m	14	29 m	26	222 m	38	1684 m
3	3 m	15	34 m	27	216 m	39	1941 m
4	5 m	16	40 m	28	318 m	40	2225 m
5	6 m	17	47 m	29	380 m	41	2533 m
6	7 m	18	55 m	30	453 m	42	2865 m
7	9 m	19	65 m	31	541 m	43	3220 m
8	11 m	20	77 m	32	643 m	44	3597 m
9	13 m	21	92 m	33	763 m	45	3992 m

Table 1. Cont.

Layer	Depth	Layer	Depth	Layer	Depth	Layer	Depth
10	15 m	22	109 m	34	902 m	46	4405 m
11	18 m	23	130 m	35	1062 m	47	4833 m
12	21 m	24	155 m	36	1245 m	48	5274 m

3. Method

Due to the characteristics of the experimental data, including large information volume, multi-source data, and a high number of grid points, the complex information carried within the data is not conducive to model learning. Simplifying the data structure for the model to learn and deriving general patterns is key to building the model in this study.

3.1. Model Construction

Currently, the encoder–decoder structure of deep learning is widely used in related fields such as computer vision, for example, the UNet model [41]. The encoding process reduces the complexity of the data features, thus decreasing computational complexity and improving the model’s learning efficiency. The decoding process converts low-resolution feature maps into high-resolution outputs to capture image details and structures, and integrates them with contextual information from the decoding stage.

The SimVP-gsta model [42] (<https://github.com/chengtan9907/OpenSTL>, accessed on 21 September 2023) builds upon the original encoder–decoder structure by adding the gsta module (spatio-temporal attention mechanism) to the decoding structure, which accelerates the model’s convergence speed and improves operational efficiency. This model has demonstrated excellent performance in various datasets, including video prediction. The structure of this model is shown in Figure 2, where Figure 2a illustrates the overall framework of the model, and Figure 2b depicts the gsta module in the decoding structure.

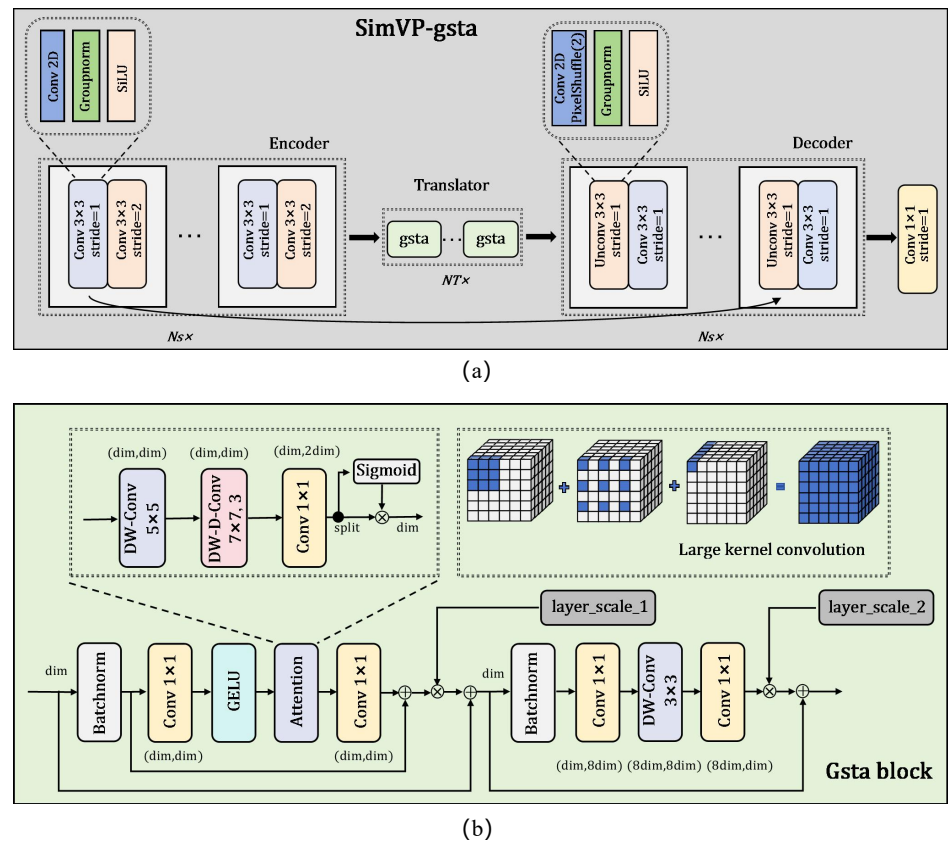


Figure 2. SimVP-gsta model. Figure (a) shows the SimVP-gsta model, and figure (b) shows the gsta module.

The improved model in this paper, M-ViT, has a structure similar to the SimVP-gsta model, featuring an encoder–translator–decoder framework. The translator is a lightweight Mobile–ViT module [43] (<https://github.com/jaiwei98/mobile-vit-pytorch>, accessed on 13 September 2023). This model performed excellently in the spatiotemporal prediction in this experiment. The specific model is shown in Figure 3, where Figure 3a depicts the overall framework of the model, and Figure 3b shows the decoder structure, which is the Mobile–ViT module.

In the experiments for constructing the intelligent forecasting and inversion models, we compared the training results of SimVP-gsta, M-ViT, and other typical models that have been used in ocean research [36,38,40,44]. The best-performing model from this comparison was selected as the foundational model for the 3D temperature and salinity forecasting model in this study.

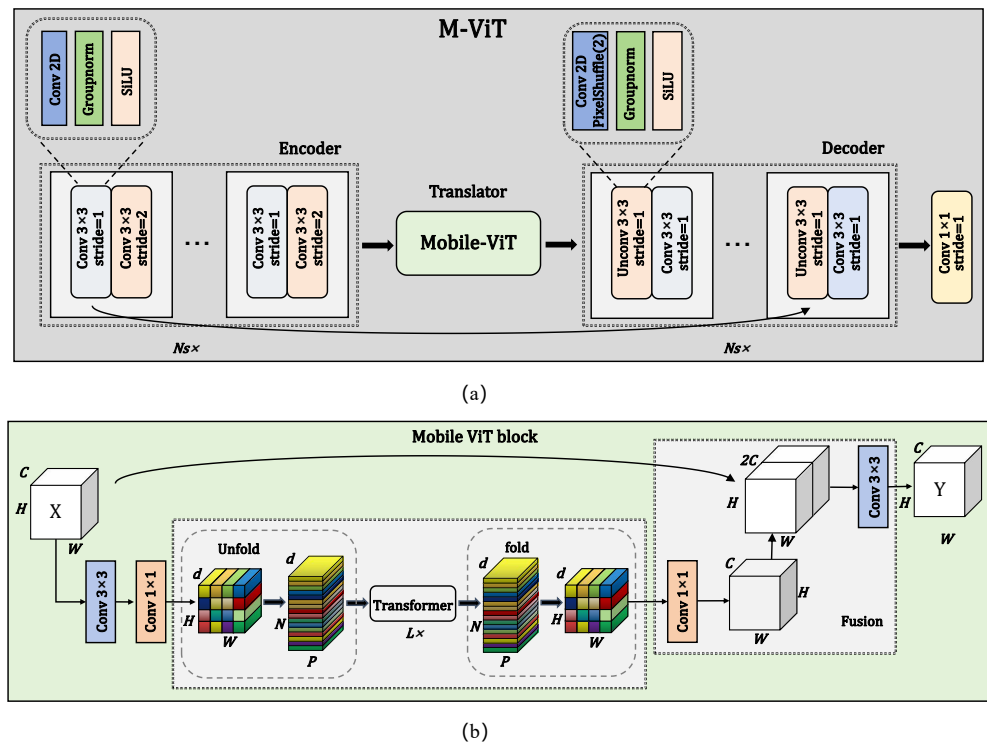


Figure 3. M-ViT model. Figure (a) shows the M-ViT model, and figure (b) shows the Mobile-ViT module.

3.2. Construction of the 3D Prediction Model

The three-dimensional temperature and salinity intelligent forecasting model is an integrated system comprising three submodels: the sea surface intelligent forecasting model, the bilinear interpolation model, and the three-dimensional temperature and salinity inversion model based on combined SST and SLA. The diagram of the three-dimensional forecasting model is shown in Figure 4. The integration method for the three-dimensional forecasting model can be implemented as follows. First, obtain the SST and SLA for the next x time steps:

$$SST_{t+1}, SST_{t+2}, \dots, SST_{t+x} = Pred_Model1(SST_{t-n}, SST_{t-n+1}, \dots, SST_t) \quad (1)$$

$$SLA_{t+1}, SLA_{t+2}, \dots, SLA_{t+x} = Pred_Model2(SLA_{t-n}, SLA_{t-n+1}, \dots, SLA_t) \quad (2)$$

where *Pred_Model1* is the SST forecasting model and *Pred_Model2* is the SLA forecasting model. Then, perform bilinear interpolation on the predicted SST and SLA for the next

x time steps and match them with the reanalysis data in both the spatial and temporal dimensions:

$$B_SST_{t+i} = Bi_Model(SST_{t+i}), i \in x \tag{3}$$

$$B_SLA_{t+i} = Bi_Model(SLA_{t+i}), i \in x \tag{4}$$

where B_SST_{t+i} and B_SLA_{t+i} represent the SST and SLA states after bilinear interpolation, respectively. The bilinear interpolation model is illustrated in Figure 5.

Assuming the data at the point (x, y) and its surrounding four points (x_0, y_0) , (x_0, y_1) , (x_1, y_0) , and (x_1, y_1) are $f(x_0, y_0)$, $f(x_0, y_1)$, $f(x_1, y_0)$, and $f(x_1, y_1)$, respectively, $f(x_0, y) = f(x_0, y_0) + y * [f(x_0, y_1) - f(x_0, y_0)]$, $f(x_1, y) = f(x_1, y_0) + y * [f(x_1, y_1) - f(x_1, y_0)]$, the bilinear interpolation is given by $f(x, y) = f(x_0, y) + x * [f(x_1, y) - f(x_0, y)]$. The interpolated SST and SLA values for the corresponding time are then jointly input into the inversion model to obtain the future subsurface temperature and salinity information:

$$ST_{t+i}, SS_{t+i} = Inv_Model(B_SST_{t+i}, B_SLA_{t+i}), i \in x \tag{5}$$

where ST_{t+i} and SS_{t+i} represent the subsurface temperature and salinity, respectively, and Inv_Model is the inversion model.

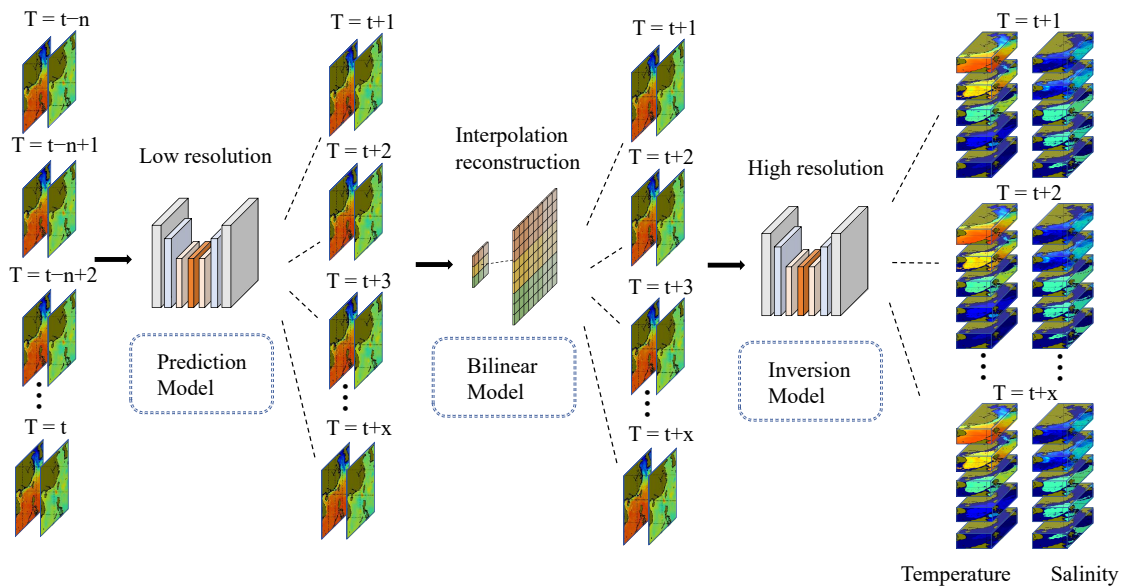


Figure 4. Three-dimensional prediction model.

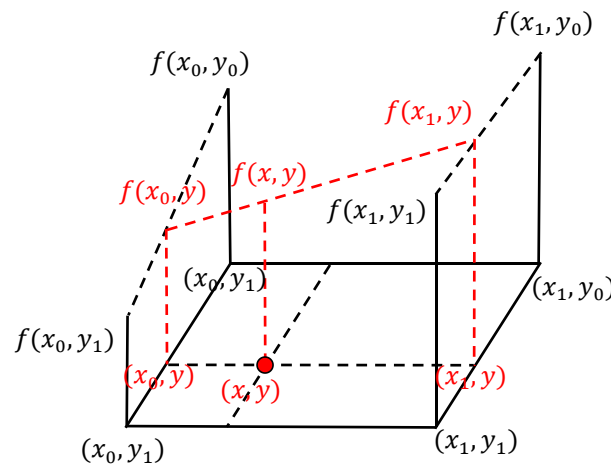


Figure 5. Bilinear interpolation model.

4. Parameter Settings and Evaluation Metrics

4.1. Parameter Settings

Before training, the input and target data are first normalized using Z-Score normalization. The forecast data are organized in the shape (B, T, H, W), where B is the batch size, T is the time step, H and W are the height and width of the data, respectively. The inversion data are organized in the shape (B, L, E, H, W), where L represents the ocean depth layers, and E is the number of input features. We provide statistics for the optimal final prediction model M-ViT and the optimal inversion model SimVP-gsta. The results are as follows. The data and model parameters are shown in Table 2. Here, “dim” represents the hidden layer dimension of the SimVP-gsta model, “NT” is the number of gsta modules, and “Ns” is the number of encoder–decoder modules. “C” denotes the hidden layer dimension of the M-ViT model, “L” is the number of Transformer layers used in the Mobile-ViT model, and “P” is the size of each data block during segmentation.

Table 2. Data and model parameter settings.

Parameter	Model						Data			
	SimVP-gsta			M-ViT			B	T(in, out)	L(in, out)	E(in, out)
	dim	N_T	N_S	C	L	P				
NWP	512	6	6	1024	6	(7, 5)	8	(30, 20)	(1, 48)	(2, 2)
CWOC	512	6	8	1024	6	(15, 9)	8	(30, 20)	(1, 48)	(2, 2)

In this prediction and inversion experiment, the MSE function was selected as the loss function. Due to the different distribution patterns of temperature and salinity, a dual loss function was used to constrain the model in the inversion experiment, capturing the distribution patterns of the temperature and salinity data. The specific scheme is shown in Figure 6. This experiment was conducted on a single NVIDIA A100 GPU (Sourced from NVIDIA Corporation in Santa Clara, CA, USA) for training. The initial learning rate for both the prediction and inversion model training was set to 0.001, and OneCycleLR was employed for learning rate updates, continuously adjusting the network’s learning rate to find the optimal solution. The number of iterations for training the network was set to 100, and the Adam optimizer was chosen.

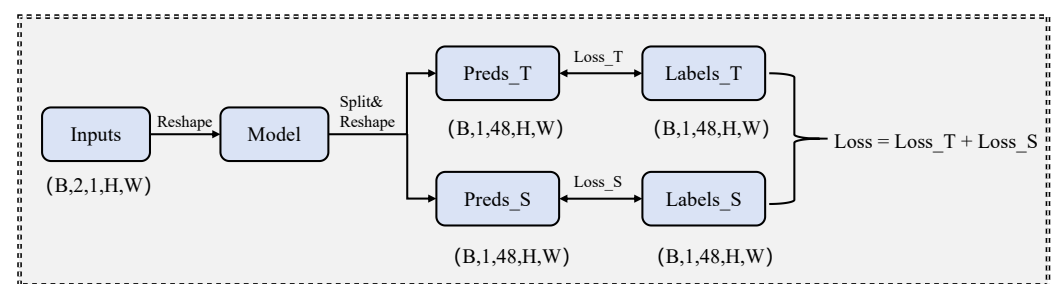


Figure 6. Loss function settings in the inversion experiment.

4.2. Evaluation Metrics

In this experiment, Mean Absolute Error (MAE) (Equation (6)) and Root Mean Squared Error (RMSE) (Equation (7)) were used as evaluation metrics for the prediction and inversion experiment results. The formulas are as follows:

$$MAE = \frac{1}{N} \sum_{i=1}^N |y_i - \hat{y}_i| \tag{6}$$

$$RMSE = \sqrt{\frac{1}{N} \sum_{i=1}^N (y_i - \hat{y}_i)^2} \tag{7}$$

In the above formula, N represents the total number of grid points in the sample, y_i denotes the observed true values, and \hat{y}_i represents the predicted values.

5. Experimental Results

5.1. SST Prediction

The experiments used satellite remote sensing SST data to construct a temperature forecasting model for the offshore areas of China and the Northwest Pacific region. Historical SST data for 30 days were input into the model to predict temperature changes for the next 20 days. The experiments were conducted under the same training conditions, comparing UNet, SimVP-gsta, M-ViT, Linear Regression Model (L-R), ViT Model [45], and ConvFormer Model [46]. The training results were tested using a test set, and the best-performing model among the compared models was selected as the foundational model for the three-dimensional temperature and salinity forecasting model. Before computing the metrics, the land areas were removed, and the period from December 2021 to November 2022 was used as the test set. The results of the tests for the two regions are presented below.

5.1.1. Coastal Waters of China

To better describe the model’s prediction ability for each time period, the 20-day error metrics were averaged every 5 days and tabulated as shown in Table 3.

Table 3. Statistical results of the 20-day SST prediction error in the Coastal Waters of China. An arrow pointing downward indicates that a lower value of the indicator is better.

Time	Average-MAE (↓)						Average-RMSE (↓)					
	Simvp-gsta	UNet	M-ViT	L-R	ConvFormer	ViT	Simvp-gsta	UNet	M-ViT	L-R	ConvFormer	ViT
1~5 days	0.3896	0.6806	0.3201	0.3457	0.4348	0.3843	0.5365	0.8299	0.4471	0.4754	0.5749	0.5292
6~10 days	0.4934	0.7585	0.4639	0.5386	0.5583	0.4894	0.6715	0.9496	0.6423	0.7525	0.7450	0.6683
11~15 days	0.5344	0.8093	0.5273	0.6840	0.6545	0.5819	0.7277	1.0182	0.7282	0.9505	0.8537	0.7720
16~20 days	0.5829	0.8554	0.5541	0.8223	0.6549	0.6454	0.7917	1.0764	0.7484	1.1411	0.8728	0.8511
Average	0.5001	0.7760	0.4664	0.5977	0.5756	0.5253	0.6819	0.9685	0.6465	0.8299	0.7616	0.7052

Analysis of the error metrics in Table 3: From the overall results of the 1–20 day forecasts, the M-ViT model demonstrates the best performance in SST prediction experiments compared to other deep learning models, with the SimVP-gsta model following. Compared to the SimVP-gsta model, the M-ViT model reduces the average MAE metric by 6.7% and the RMSE metric by 5.2% for the 20-day forecast. The linear regression model exhibits smaller prediction errors in the 1–5 day time range; however, its forecast error growth rate is the largest as time increases. To more intuitively express the test results, the error metrics over the 20 days are visualized for comparison (as shown in Figure 7). The figure clearly shows that the M-ViT model has the best predictive performance.

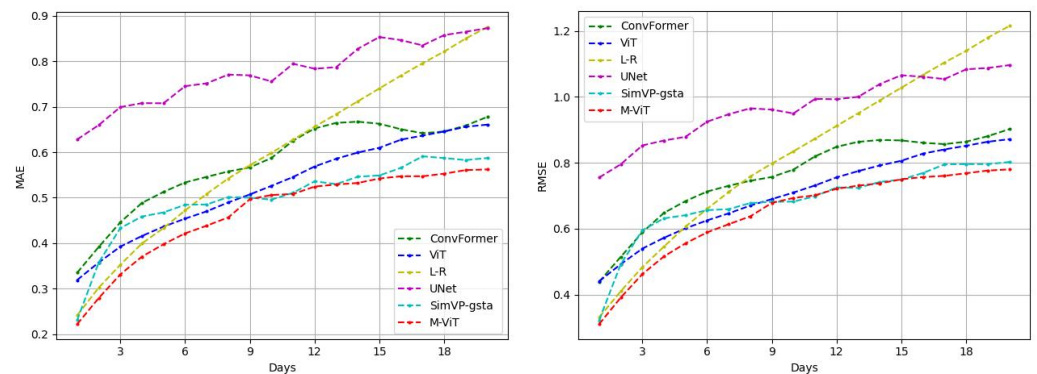


Figure 7. Visualization of the average SST prediction error over 20 days in the Coastal Waters of China. The MAE chart is on the left, and the RMSE chart is on the right.

5.1.2. Northwest Pacific

Analysis of the error metrics in Table 4: The M-ViT model demonstrates better results compared to other prediction models, exhibiting lower overall MAE and RMSE. Specifically, compared to the SimVP-gsta model, the M-ViT model reduces the average MAE by 4.6% and the RMSE by 3.2% over the 20-day forecast period. The errors over these 20 days are visualized for comparison (as shown in Figure 8), where it is evident that the M-ViT model consistently maintains the best predictive performance throughout the entire period.

Table 4. Statistical results of the 20-day SST prediction error in the Northwest Pacific. An arrow pointing downward indicates that a lower value of the indicator is better.

Time	Average-MAE (↓)						Average-RMSE (↓)					
	Simvp-gsta	UNet	M-ViT	L-R	ConvFormer	ViT	Simvp-gsta	UNet	M-ViT	L-R	ConvFormer	ViT
1~5 days	0.2972	0.5027	0.2782	0.2989	0.6730	0.3286	0.4368	0.6538	0.4793	0.4529	0.8441	0.4902
6~10 days	0.4347	0.5829	0.4182	0.4960	0.7463	0.4446	0.6441	0.7810	0.6279	0.7432	0.9737	0.6556
11~15 days	0.5099	0.6422	0.4884	0.6297	0.7899	0.5093	0.7537	0.8681	0.7314	0.9408	1.0542	0.7467
16~20 days	0.5698	0.7034	0.5425	0.7603	0.8438	0.5642	0.8452	0.9491	0.8156	1.1395	1.1062	0.8261
Average	0.4529	0.6078	0.4318	0.5462	0.7558	0.4617	0.6700	0.8130	0.6486	0.8191	0.9946	0.6797

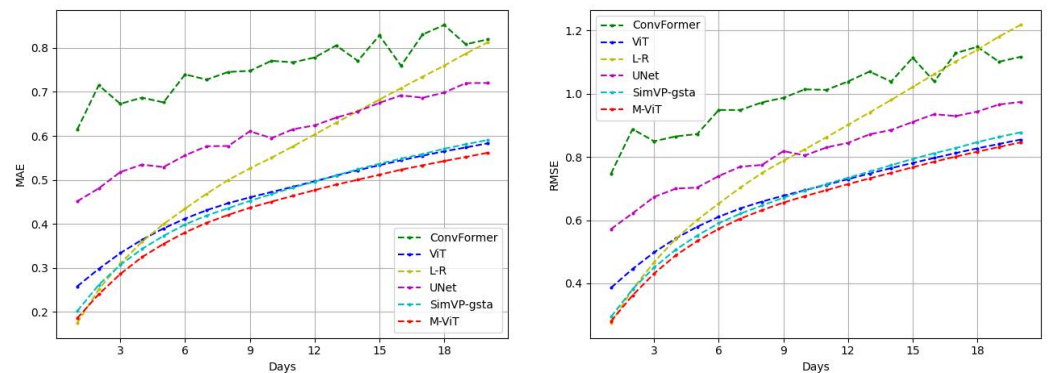


Figure 8. Visualization of the average SST prediction error over 20 days in the Northwest Pacific. The MAE chart is on the left, and the RMSE chart is on the right.

From the experimental results of the above two sea regions, it can be concluded that the M-ViT model exhibits the best predictive performance in overall temperature prediction. Therefore, this paper uses the M-ViT model as the base model for temperature prediction in the 3D temperature and salinity prediction experiment.

5.2. SLA Prediction

Thirty days of historical SLA data were input into the models to predict the changes in SLA for the next 20 days. The testing procedures were the same as in the SST prediction experiments. The following are the results of the tests conducted separately for the two sea areas. The models used for training in this section were the same as those used in the SST forecasting model.

5.2.1. Coastal Waters of China

To better describe the predictive capabilities of each model in each time period, we averaged the 20-day error metrics every 5 days and present them in a table as shown in Table 5.

Analysis of the error metrics in Table 5: The M-ViT model outperformed other deep learning models in predicting SLA, demonstrating the best overall performance. Compared to the SimVP-gsta model, the M-ViT model provided slightly better results, reducing the average MAE by 1.8% and the RMSE by 1.1% over the 20-day forecast period. The errors over these 20 days are visualized for comparison (as shown in Figure 9), where it can be seen that the M-ViT model delivers superior prediction results.

Table 5. Statistical results of the 20-day SLA prediction error in the Coastal Waters of China. An arrow pointing downward indicates that a lower value of the indicator is better.

Time	Average-MAE (↓)						Average-RMSE (↓)					
	Simvp-gsta	UNet	M-ViT	L-R	ConvFormer	ViT	Simvp-gsta	UNet	M-ViT	L-R	ConvFormer	ViT
1~5 days	0.0229	0.0429	0.0224	0.0327	0.0327	0.0281	0.0320	0.0546	0.0317	0.0385	0.0431	0.0378
6~10 days	0.0368	0.0523	0.0363	0.0506	0.0455	0.0441	0.0510	0.0674	0.0507	0.0687	0.0601	0.0587
11~15 days	0.0441	0.0589	0.0431	0.0619	0.0524	0.0548	0.0602	0.0761	0.0593	0.0816	0.0692	0.0715
16~20 days	0.0484	0.0647	0.0476	0.0694	0.0563	0.0614	0.0658	0.0829	0.0652	0.0903	0.0745	0.0797
Average	0.0381	0.0547	0.0374	0.0526	0.0467	0.0471	0.0523	0.0703	0.0517	0.0698	0.0617	0.0619

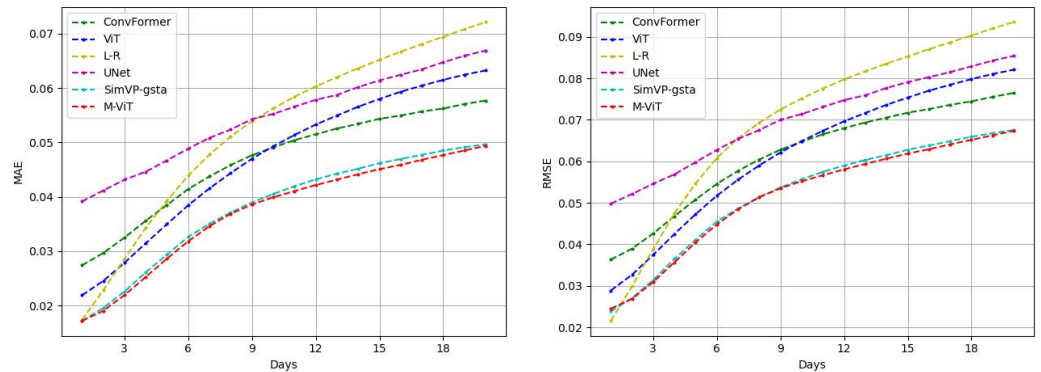


Figure 9. Visualization of the average SLA prediction error over 20 days in the Coastal Waters of China. The MAE chart is on the left, and the RMSE chart is on the right.

5.2.2. Northwest Pacific

Analysis of the error metrics in Table 6: The M-ViT and SimVP-gsta models provide better average prediction results over the 20-day period compared to other prediction models. Specifically, the SimVP-gsta model performs better in terms of average prediction accuracy for the 1–5 day range, while the M-ViT model has an advantage in the 6–20 day range. The error metrics over the 20 days are visualized for comparison (as shown in Figure 10). Figure 10 shows that the linear regression model has lower errors in short-term predictions but performs poorly in medium- to long-term forecasts.

Table 6. Statistical results of the 20-day SLA prediction error in the Northwest Pacific. An arrow pointing downward indicates that a lower value of the indicator is better.

Time	Average-MAE (↓)						Average-RMSE (↓)					
	Simvp-gsta	UNet	M-ViT	L-R	ConvFormer	ViT	Simvp-gsta	UNet	M-ViT	L-R	ConvFormer	ViT
1~5 days	0.0213	0.0402	0.0235	0.0214	0.0507	0.0203	0.0303	0.0504	0.0326	0.0354	0.0544	0.0300
6~10 days	0.0327	0.0466	0.0327	0.0396	0.0507	0.0329	0.0470	0.0608	0.0464	0.0636	0.0648	0.0467
11~15 days	0.0416	0.0527	0.0408	0.0521	0.0568	0.0429	0.0606	0.0714	0.0587	0.0813	0.0756	0.0609
16~20 days	0.0476	0.0578	0.0467	0.0607	0.0611	0.0503	0.0702	0.0801	0.0680	0.0932	0.0840	0.0715
Average	0.0351	0.0493	0.0359	0.0435	0.0548	0.0366	0.0520	0.0657	0.0514	0.0684	0.0697	0.0523

Based on the results of the two sea area experiments mentioned above, the M-ViT model demonstrates the best predictive performance in overall SLA predictions. Therefore, this paper will use the M-ViT model as the baseline model for SLA predictions in the 3D temperature and salinity prediction experiments.

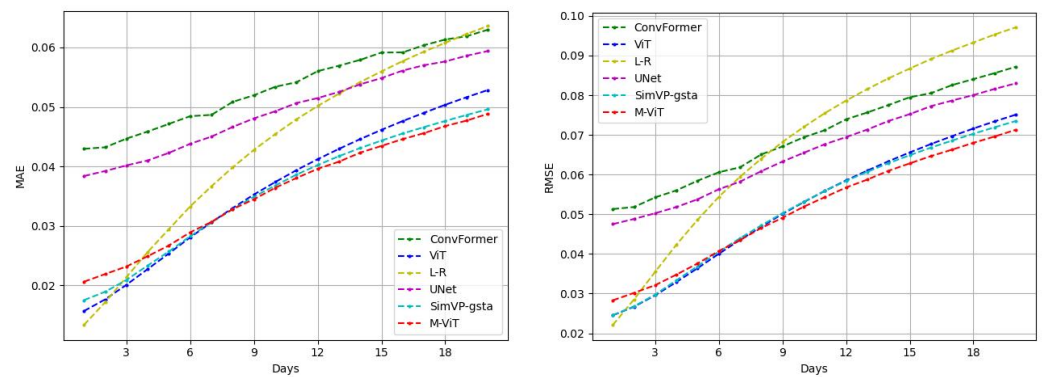


Figure 10. Visualization of the average SLA prediction error over 20 days in the Northwest Pacific. The MAE chart is on the left, and the RMSE chart is on the right.

5.3. Ocean Subsurface Temperature and Salinity Vertical Inversion

The experiment first performed bilinear interpolation on the historical SST and SLA data at a $1/4^\circ$ resolution from satellite remote sensing. These interpolated data were then matched spatially with $1/12^\circ$ resolution reanalysis temperature and salinity data. These combined data sources were used to construct a subsurface temperature and salinity inversion model for the Chinese coastal and Northwest Pacific regions. The interpolated historical SST data and SLA data were combined and input into the model to retrieve temperature and salinity data for 48 layers below the sea surface (approximately 5000 m deep). Under the same training conditions, models including UNet, SimVP-gsta, M-ViT, ConvFormer, Atten-UNet, and ViT were trained simultaneously. The training results were evaluated using a test set, with the best-performing model among the compared models chosen as the base model for the three-dimensional temperature and salinity forecasting model. Before calculating the metrics, the land areas were excluded, and the period from December 2021 to November 2022 was used as the test set. The following are the test results for the two regions.

5.3.1. Coastal Waters of China

Due to the different distribution characteristics of temperature and salinity at various subsurface layers, the error metrics of the three models' predictions were averaged separately for depths shallower than 600 m and deeper than 600 m. The results were then tabulated as shown in Table 7.

Analysis of Error Metrics in Table 7: The SimVP-gsta model outperformed other deep learning models overall in the temperature and salinity vertical inversion experiments. For temperature inversion, the results of the SimVP-gsta and M-ViT models are comparable, with SimVP-gsta being slightly better. However, in the salinity inversion, the SimVP-gsta model significantly outperformed the other models. The M-ViT model exhibited smaller errors at depths shallower than 600 m, but at depths greater than 600 m, it struggled to capture salinity distribution characteristics, leading to a noticeable increase in errors.

Table 7. Statistical results of vertical temperature and salinity inversion errors in the Coastal Waters of China. An arrow pointing downward indicates that a lower value of the indicator is better.

Element	Depth	Average-MAE (↓)						Average-RMSE (↓)					
		Simvp-gsta	UNet	M-ViT	Atten-UNet	ConvFormer	ViT	Simvp-gsta	UNet	M-ViT	Atten-UNet	ConvFormer	ViT
Temp	<600 m	0.4969	0.7577	0.5099	0.6807	0.7933	0.5391	0.6968	1.0916	0.7192	0.9986	1.0385	0.7881
	>600 m	0.1017	0.1605	0.1086	0.1565	0.1550	0.1368	0.1467	0.2686	0.1535	0.2678	0.2171	0.1929
Sal	<600 m	0.2106	0.4183	0.2393	0.3512	0.3725	0.3282	0.3261	0.9422	0.3865	0.8816	0.5516	0.6021
	>600 m	0.0690	0.4586	0.1162	0.2295	0.3714	0.2361	0.0937	1.0096	0.3063	0.9580	0.5176	0.4784

To better illustrate the inversion results, the error metrics for the 48-layer temperature and salinity inversions are visualized for comparison (as shown in Figure 11). Figure 11

shows that under the same experimental conditions, the SimVP-gsta model achieved the best overall results in temperature and salinity inversion. While many models tend to learn the temperature distribution pattern but struggle to simultaneously learn both temperature and salinity distribution patterns, the SimVP-gsta model excels at learning both. This balanced learning capability makes the SimVP-gsta model superior in terms of overall performance.

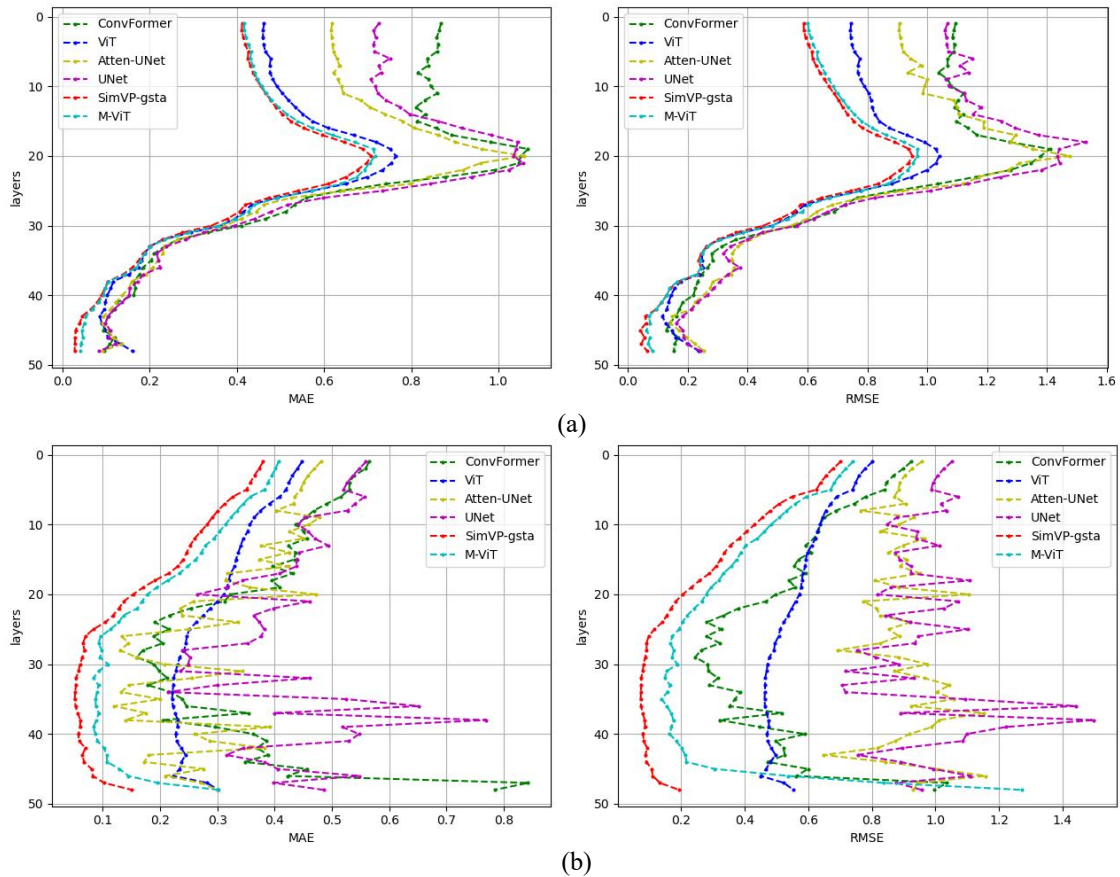


Figure 11. Visualization of errors in 48-layer temperature and salinity inversion in the Coastal Waters of China. Figure (a) represents the temperature error, with the MAE chart on the left and the RMSE chart on the right. Figure (b) represents the salinity error, with the MAE chart on the left and the RMSE chart on the right.

5.3.2. Northwest Pacific

Analysis of error metrics in Table 8: In terms of overall performance, the SimVP-gsta model excels in both temperature and salinity inversion. The M-ViT model also demonstrated strong inversion performance for temperature, but it exhibited larger errors in salinity inversion, particularly at depths greater than 600 m, where it struggled to maintain a balanced learning of salinity patterns.

Table 8. Statistical results of vertical temperature and salinity inversion errors in the Northwest Pacific. An arrow pointing downward indicates that a lower value of the indicator is better.

Element	Depth	Average-MAE (↓)						Average-RMSE (↓)					
		Simvp-gsta	UNet	M-ViT	Atten-UNet	ConvFormer	ViT	Simvp-gsta	UNet	M-ViT	Atten-UNet	ConvFormer	ViT
Temp	<600 m	0.5134	0.6684	0.5761	0.7873	0.8208	0.8823	0.7587	0.9567	0.8438	1.1241	1.1698	1.3008
	>600 m	0.0975	0.1201	0.1101	0.1785	0.1585	0.1735	0.1377	0.1786	0.1590	0.3003	0.2503	0.2826
Sal	<600 m	0.1935	0.2661	0.2440	0.4037	0.3960	0.3935	0.3192	0.3682	0.4244	0.7596	0.6607	0.6035
	>600 m	0.1025	0.1311	0.2381	0.3208	0.2585	0.3357	0.2443	0.2527	0.4647	0.7050	0.5442	0.6079

The error metrics for the 48-layer temperature and salinity inversions are visualized for comparison (as shown in Figure 12). Figure 12 illustrates that, under the same experimental conditions, the SimVP-gsta model outperformed other deep learning models in overall inversion results. Although the UNet model showed relatively small errors in salinity inversion, it still experienced error fluctuations. Most models exhibited an imbalance in learning salinity, indicating that they find it challenging to simultaneously capture the distribution patterns of both temperature and salinity. In contrast, the SimVP-gsta model delivered better inversion results, demonstrating superior model performance.

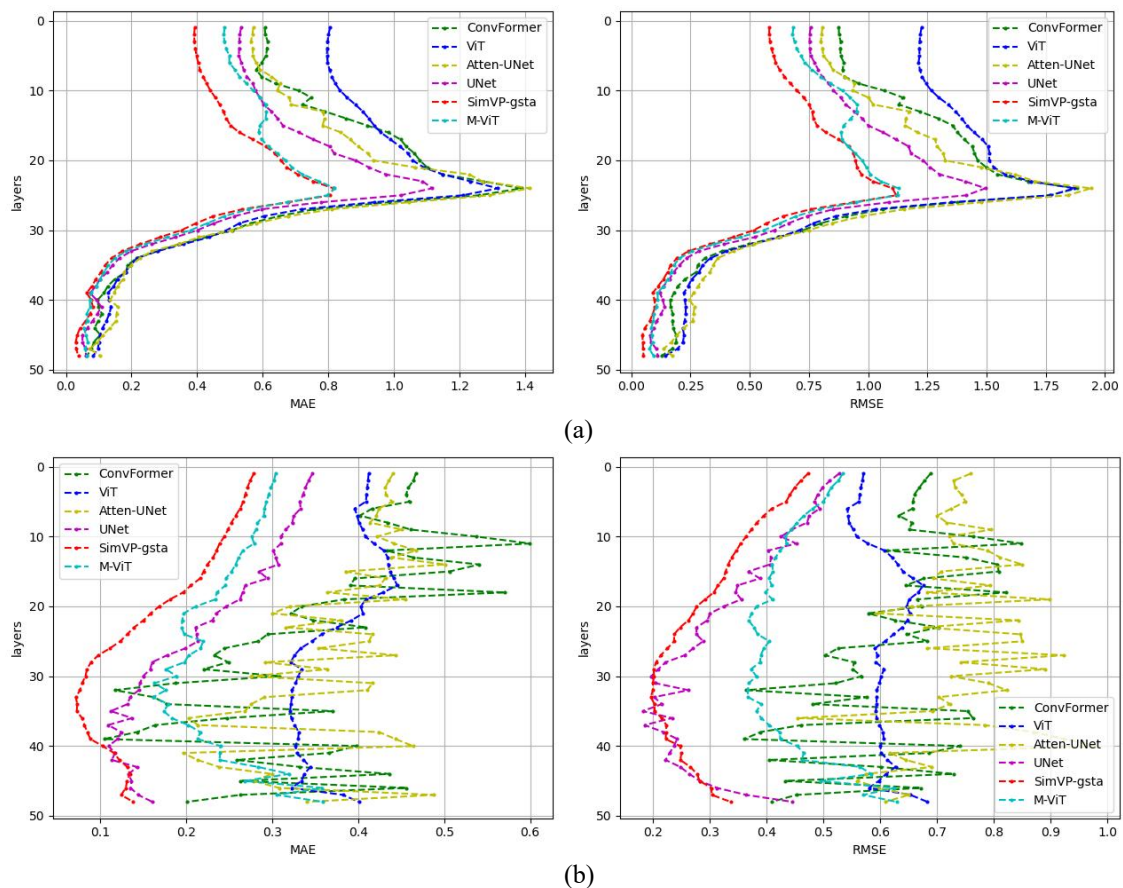


Figure 12. Visualization of errors in 48-layer temperature and salinity inversion in the Northwest Pacific. Figure (a) represents the temperature error, with the MAE chart on the left and the RMSE chart on the right. Figure (b) represents the salinity error, with the MAE chart on the left and the RMSE chart on the right.

Based on the results of the two sea area experiments mentioned above, the SimVP-gsta model demonstrated the best performance in overall temperature and salinity vertical inversion. Therefore, this paper will use the SimVP-gsta model as the baseline model for temperature and salinity inversion in the 3D temperature and salinity prediction experiments.

5.4. Three-Dimensional Temperature and Salinity Prediction

In this section, we integrate the SST prediction model, the SLA prediction model, and the ocean subsurface vertical inversion model to develop a 3D temperature and salinity prediction model for the ocean subsurface. To optimize the prediction performance, the best models from the above experiments were chosen as the foundational models for the 3D prediction model. The basic prediction steps are as follows: first, input the 1/4° SST data and SLA data into the M-ViT model to obtain 20-day prediction data. Then, apply bilinear interpolation to the prediction data and input them into the inversion model,

the SimVP-gsta model, to obtain the final high-resolution 3D temperature and salinity prediction results.

To effectively test the prediction results while maintaining seasonal continuity, the period from December 2021 to November 2022 was selected as the test dataset. The data were divided into four quarters for testing and statistics: winter (December–February), spring (March–May), summer (June–August), and autumn (September–November). Before calculating the metrics, the land areas were excluded, and the data from the entire year of 2022 were used as the test set. The following are the test results for the two specific sea areas.

5.4.1. Coastal Waters of China

The average of the 20-day prediction results for each prediction within the entire quarter was calculated, and then the 20-day prediction results were averaged every 5 days. The statistical results are shown in Table 9.

Table 9. Statistical results of the 20-day 3D temperature and salinity prediction errors in the Coastal Waters of China. An arrow pointing downward indicates that a lower value of the indicator is better.

Time	Element	Depth	Average-MAE (↓)				Average-RMSE (↓)			
			Winter	Spring	Summer	Autumn	Winter	Spring	Summer	Autumn
1~5 days	Temp	<600 m	0.5697	0.5463	0.6002	0.4950	0.7392	0.7420	0.7135	0.6989
		>600 m	0.1088	0.1107	0.1045	0.1043	0.1529	0.1562	0.1513	0.1536
	Sal	<600 m	0.2018	0.1897	0.1945	0.2485	0.3358	0.2998	0.2893	0.3664
		>600 m	0.0609	0.0622	0.0587	0.0565	0.0829	0.0838	0.0791	0.0765
6~10 days	Temp	<600 m	0.5818	0.5745	0.5231	0.5160	0.7611	0.7782	0.7432	0.7269
		>600 m	0.1106	0.1104	0.1042	0.1052	0.1554	0.1561	0.1511	0.1551
	Sal	<600 m	0.2047	0.1916	0.1967	0.2479	0.3392	0.3024	0.2958	0.3711
		>600 m	0.0584	0.0599	0.0567	0.0564	0.0790	0.0810	0.0766	0.0764
11~15 days	Temp	<600 m	0.5926	0.5954	0.5454	0.5333	0.7836	0.8042	0.7743	0.7495
		>600 m	0.1124	0.1107	0.1044	0.1061	0.1577	0.1567	0.1515	0.1564
	Sal	<600 m	0.2075	0.1924	0.2010	0.2496	0.3420	0.3026	0.3035	0.3754
		>600 m	0.0581	0.0592	0.0560	0.0555	0.0786	0.0802	0.0758	0.0753
16~20 days	Temp	<600 m	0.6116	0.6136	0.5660	0.5531	0.8135	0.8225	0.8027	0.7775
		>600 m	0.1143	0.1225	0.1051	0.1062	0.1598	0.1711	0.1526	0.1565
	Sal	<600 m	0.2104	0.1930	0.2068	0.2537	0.3461	0.3036	0.3117	0.3797
		>600 m	0.0582	0.0585	0.0559	0.0562	0.0790	0.0792	0.0758	0.0763

Further analysis of Table 9 reveals that, during the 1–20 day prediction period, the temperature and salinity prediction errors gradually increased over time, which is consistent with the objective laws. By comparing the prediction errors from days 1 to 5 with those from days 16 to 20, the feasibility of this 3D prediction model can be analyzed.

For the 1–5 day prediction, the average MAE for temperature at depths less than 600 m ranges between 0.4950 °C and 0.5697 °C, and the average RMSE ranges between 0.6989 °C and 0.7392 °C. At depths greater than 600 m, the average MAE ranges between 0.1043 °C and 0.1107 °C, and the average RMSE ranges between 0.1513 °C and 0.1562 °C. For the 16–20 day prediction, the average MAE for temperature at depths less than 600 m ranges between 0.5531 °C and 0.6136 °C, and the average RMSE ranges between 0.7775 °C and 0.8225 °C. At depths greater than 600 m, the average MAE ranges between 0.1051 °C and 0.1225 °C, and the average RMSE ranges between 0.1526 °C and 0.1711 °C. Compared to the 1–5 day prediction, the average MAE and RMSE for temperatures at depths less than 600 m increase by about 0.10. At depths greater than 600 m, the average MAE and RMSE increase by about 0.06.

The average MAE for salinity predictions from 1 to 5 days ranges between 0.1897 psu and 0.2485 psu for depths less than 600 m, and the average RMSE ranges between 0.2893 psu and 0.3664 psu. For depths greater than 600 m, the average MAE ranges between 0.0565 psu

and 0.0622 psu, and the average RMSE ranges between 0.0765 psu and 0.0838 psu. For salinity predictions from 16 to 20 days, the average MAE for depths less than 600 m ranges between 0.1930 psu and 0.2537 psu, and the average RMSE ranges between 0.3036 psu and 0.3797 psu. For depths greater than 600 m, the average MAE ranges between 0.0559 psu and 0.0562 psu, and the average RMSE ranges between 0.0580 psu and 0.0792 psu. Compared to the 1–5 day predictions, the average MAE and RMSE for salinity at depths less than 600 m increase by about 0.02, while the salinity error at depths greater than 600 m shows a negative growth. This is because, during the backpropagation process in deep learning, the model tends to focus on areas with larger losses, and the salinity error at depths greater than 600 m is relatively small. This causes the model to emphasize the salinity distribution at depths less than 600 m, leading to a lack of consistency.

To further analyze the characteristics of the predictions in each season, the temperature and salinity error data in Table 9 were plotted in 48 layers as shown in Figures 13 and 14.

From Figure 13, it can be observed that during autumn (September–November), the temperature prediction accuracy is higher above the thermocline. However, the largest errors at the thermocline occur during autumn, indicating that autumn is a complex, variable, and unstable transition period [47,48]. Figure 14 shows that in salinity predictions, the errors in autumn are consistently larger at depths less than 600 m. Beyond 600 m, the model tends to focus on areas with larger errors during training, resulting in no significant differences in salinity distribution among the four seasons within this depth range. From the error trends, it can be seen that the temperature and salinity forecast results closely match the trend of the SimVP-gsta model’s inversion results, indicating that the fundamental model determines the basic performance of the three-dimensional forecasting model.

Based on the overall error analysis, it can be concluded that the prediction method proposed in this paper has strong robustness in capturing the patterns of temperature and salinity distribution. To more intuitively display the prediction results, the 48-layer prediction results for the 1st and 20th days were selected, and the 5th, 15th, 25th, 35th, and 45th layers were visualized. Additionally, the absolute error plot for each layer was drawn as shown in Figures 15 and 16. From the figures, it can be seen that the proposed method can effectively predict the 3D temperature and salinity for 20 days, demonstrating strong reliability in the prediction results.

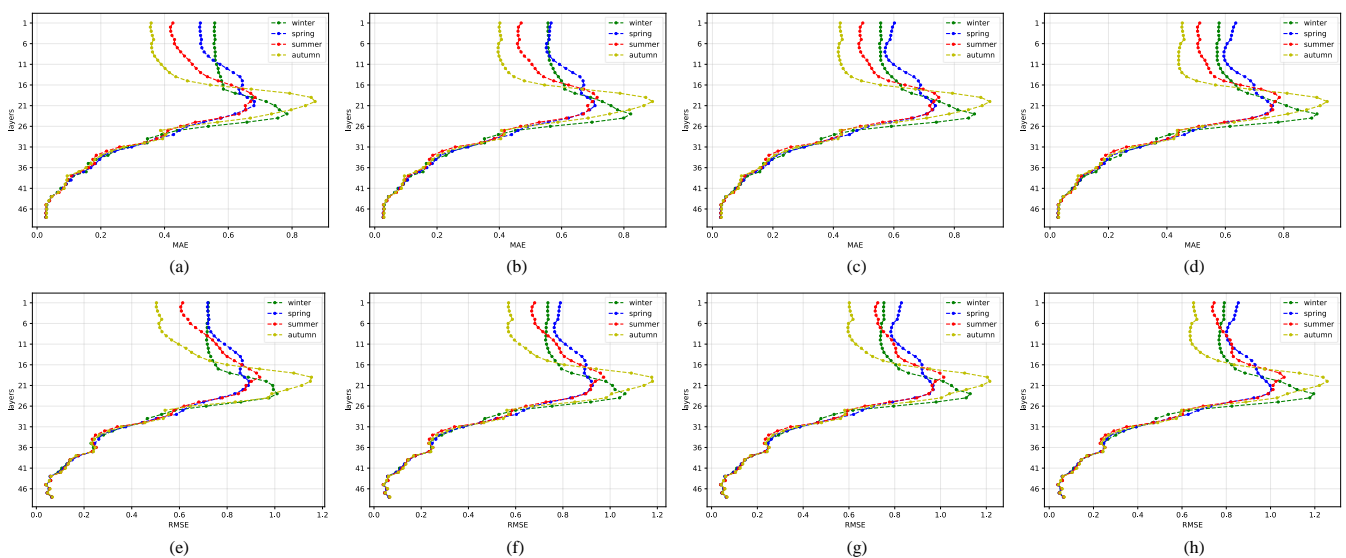


Figure 13. Three-dimensional sea temperature prediction error curves in the Coastal Waters of China. Figures (a–d) show the average MAE for temperature every 5 days from 1 to 20 days, and figures (e–h) show the average RMSE for temperature.

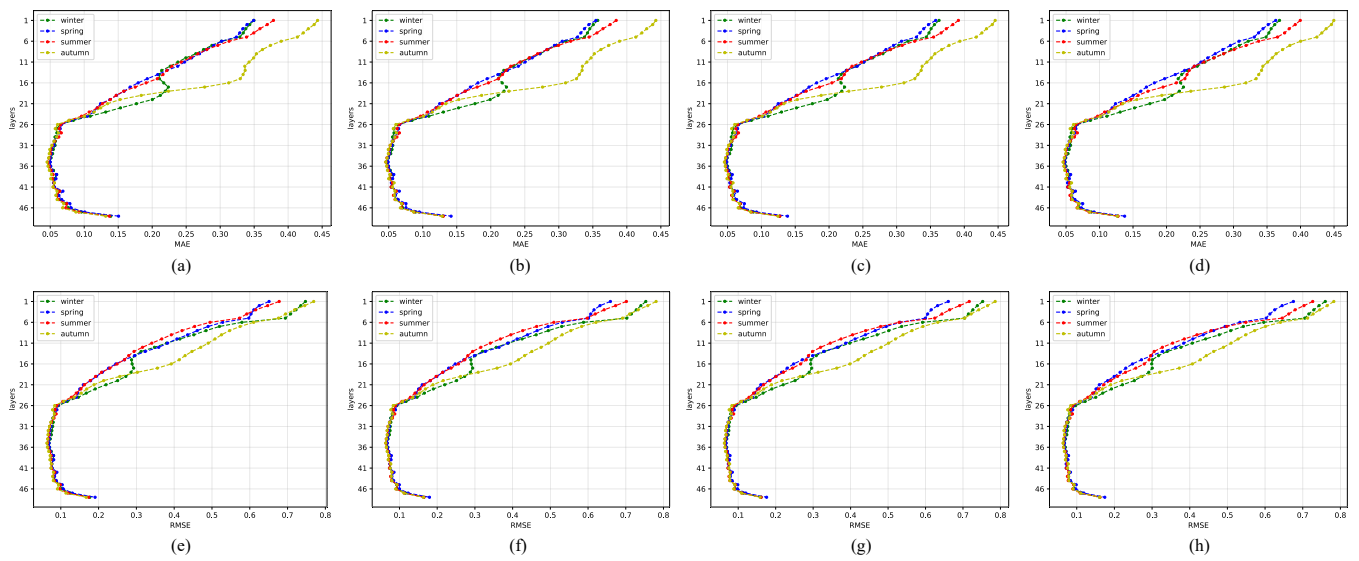


Figure 14. Three-dimensional salinity prediction error curves in the Coastal Waters of China. Figures (a–d) show the average MAE for salinity, and figures (e–h) show the average RMSE for salinity.

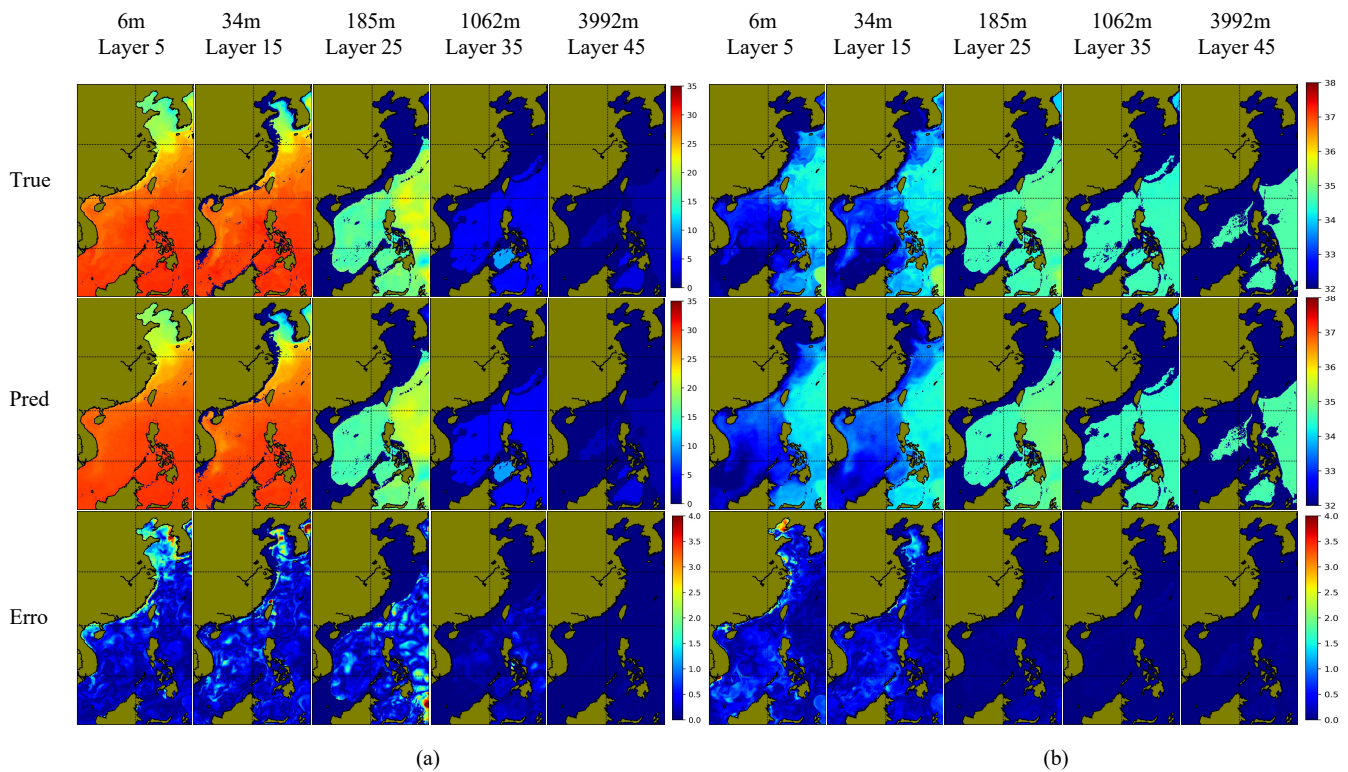


Figure 15. Visualization of the 3D temperature and salinity predictions for day 1 in the Coastal Waters of China. (a) Temperature, (b) salinity.

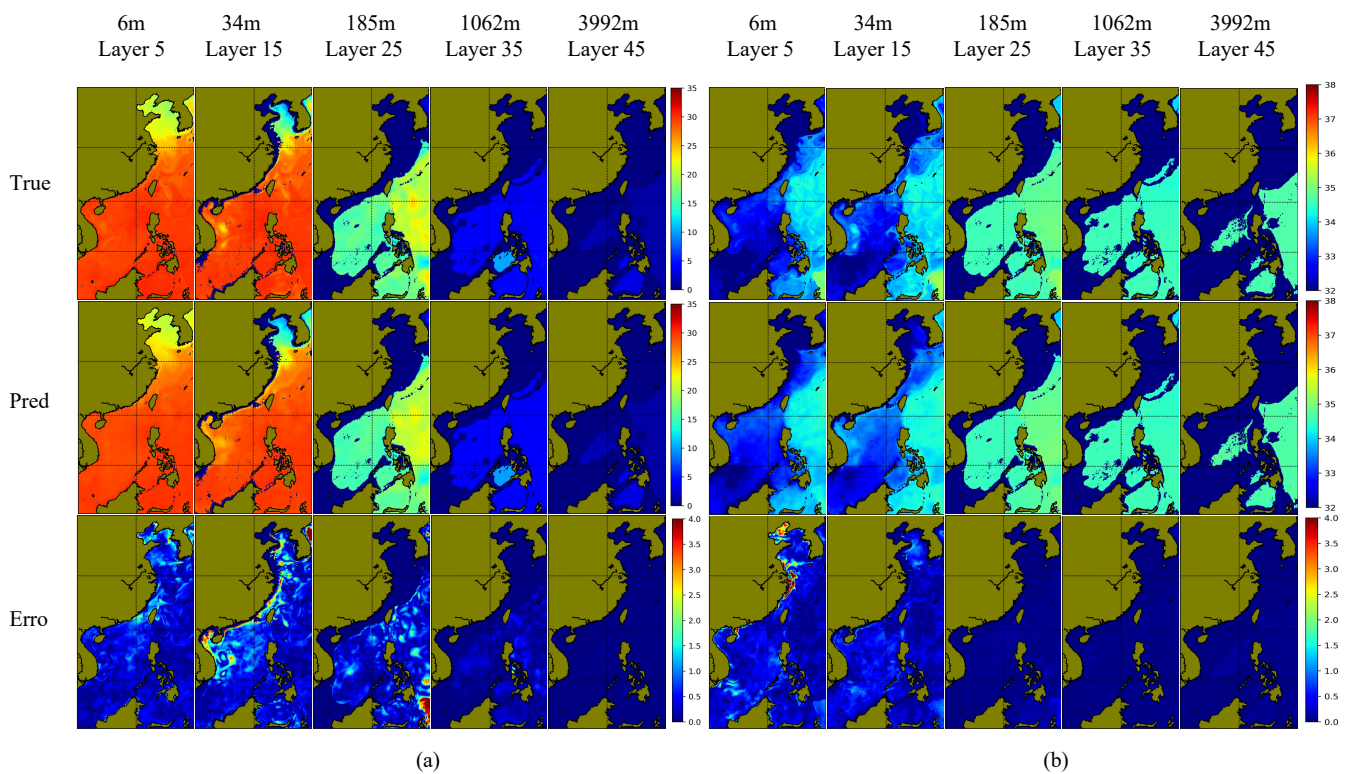


Figure 16. Visualization of the 3D temperature and salinity predictions for day 20 in the Coastal Waters of China. (a) Temperature, (b) salinity.

5.4.2. Northwest Pacific

According to Table 10, the average MAE for temperature predictions from 1 to 5 days ranges between 0.4777 °C and 0.5583 °C for depths less than 600 m, with the average RMSE ranging between 0.6896 °C and 0.8370 °C. For depths greater than 600 m, the average MAE ranges between 0.0836 °C and 0.0883 °C, with the average RMSE ranging between 0.1164 °C and 0.1226 °C. For temperature predictions from 16 to 20 days, the average MAE for depths less than 600 m ranges between 0.5378 °C and 0.6385 °C, with the average RMSE ranging between 0.7910 °C and 0.9503 °C. For depths greater than 600 m, the average MAE ranges between 0.0872 °C and 0.0904 °C, with the average RMSE ranging between 0.1216 °C and 0.1261 °C. Compared to the 1–5 day predictions, the average MAE and RMSE for temperature at depths less than 600 m both increase by about 0.14, while the average MAE and RMSE at depths greater than 600 m both increase by about 0.03.

The average MAE for salinity predictions from 1 to 5 days ranges between 0.1609 psu and 0.2088 psu for depths less than 600 m, with the average RMSE ranging between 0.2381 psu and 0.2996 psu. For depths greater than 600 m, the average MAE ranges between 0.0765 psu and 0.0934 psu, with the average RMSE ranging between 0.1229 psu and 0.1416 psu. For salinity predictions from 16 to 20 days, the average MAE for depths less than 600 m ranges between 0.1636 psu and 0.2097 psu, with the average RMSE ranging between 0.2417 psu and 0.3044 psu. For depths greater than 600 m, the average MAE ranges between 0.0780 psu and 0.0850 psu, with the average RMSE ranging between 0.1233 psu and 0.1357 psu. Compared to the 1–5 day predictions, the average MAE and RMSE for salinity at depths less than 600 m both increase by about 0.01.

To further analyze the characteristics of the predictions in each season, the temperature and salinity error data in Table 10 were plotted in 48 layers as shown in Figures 17 and 18.

Table 10. Statistical results of the 20-day 3D temperature and salinity prediction errors in the Northwest Pacific. An arrow pointing downward indicates that a lower value of the indicator is better.

Time	Element	Depth	Average-MAE (↓)				Average-RMSE (↓)			
			Winter	Spring	Summer	Autumn	Winter	Spring	Summer	Autumn
1~5 days	Temp	<600 m	0.4834	0.4777	0.5532	0.5583	0.7002	0.6896	0.8197	0.8370
		>600 m	0.0842	0.0836	0.0850	0.0883	0.1165	0.1164	0.1174	0.1226
	Sal	<600 m	0.1759	0.1609	0.1872	0.2088	0.2600	0.2381	0.2668	0.2996
		>600 m	0.0820	0.0765	0.0796	0.0934	0.1280	0.1252	0.1229	0.1416
6~10 days	Temp	<600 m	0.4980	0.5042	0.5787	0.5808	0.7264	0.7241	0.8539	0.8653
		>600 m	0.0850	0.0844	0.0854	0.0887	0.1178	0.1177	0.1180	0.1231
	Sal	<600 m	0.1746	0.1609	0.1888	0.2081	0.2590	0.2384	0.2704	0.3002
		>600 m	0.0827	0.0765	0.0792	0.0896	0.1286	0.1246	0.1254	0.1376
11~15 days	Temp	<600 m	0.5176	0.5360	0.6083	0.6059	0.7570	0.7702	0.8997	0.9013
		>600 m	0.0862	0.0858	0.0863	0.0895	0.1199	0.1200	0.1195	0.1244
	Sal	<600 m	0.1732	0.1618	0.1913	0.2085	0.2580	0.2392	0.2745	0.3016
		>600 m	0.0818	0.0768	0.0785	0.0867	0.1283	0.1224	0.1249	0.1338
16~20 days	Temp	<600 m	0.5378	0.5655	0.6385	0.6310	0.7910	0.8146	0.9503	0.9429
		>600 m	0.0876	0.0872	0.0875	0.0904	0.1225	0.1229	0.1216	0.1261
	Sal	<600 m	0.1724	0.1636	0.1941	0.2097	0.2576	0.2417	0.2786	0.3044
		>600 m	0.0806	0.0780	0.0783	0.0850	0.1270	0.1249	0.1233	0.1357

Based on Figures 17 and 18, it can be observed that autumn exhibits the highest overall errors, further indicating its complexity and variability in temperature and salinity distribution. To provide a more intuitive display of the prediction results, the 48-layer prediction results for days 1 and 20 were selected. From these, the 5th, 15th, 25th, 35th, and 45th layers were chosen for visualization. Additionally, absolute error plots were generated for each layer as depicted in Figures 19 and 20.

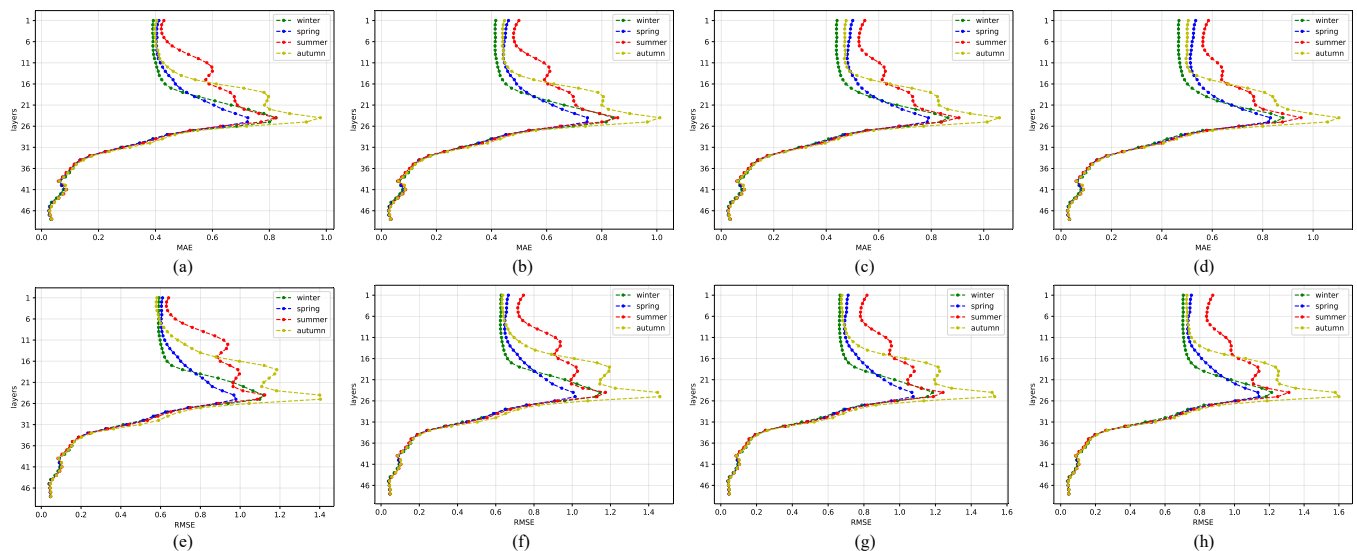


Figure 17. Three-dimensional sea temperature prediction error curves in the Northwest Pacific. Figures (a–d) show the average MAE for temperature every 5 days from 1 to 20 days, and figures (e–h) show the average RMSE for temperature.

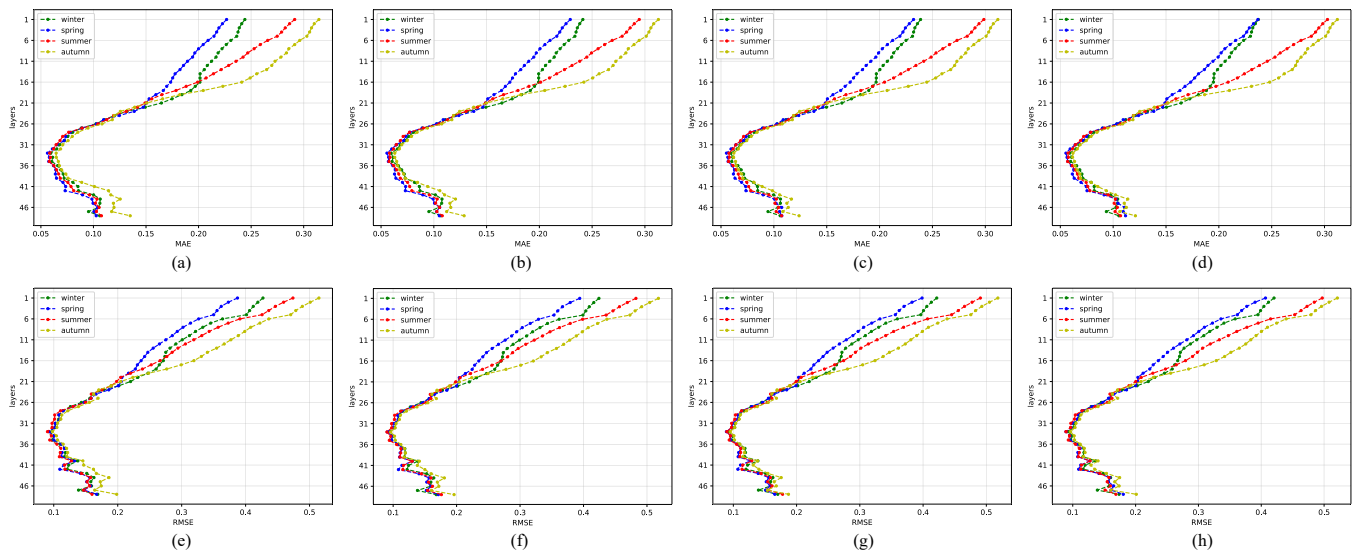


Figure 18. Three-dimensional sea salinity prediction error curves in the Northwest Pacific. Figures (a–d) show the average MAE for salinity, and figures (e–h) show the average RMSE for salinity.

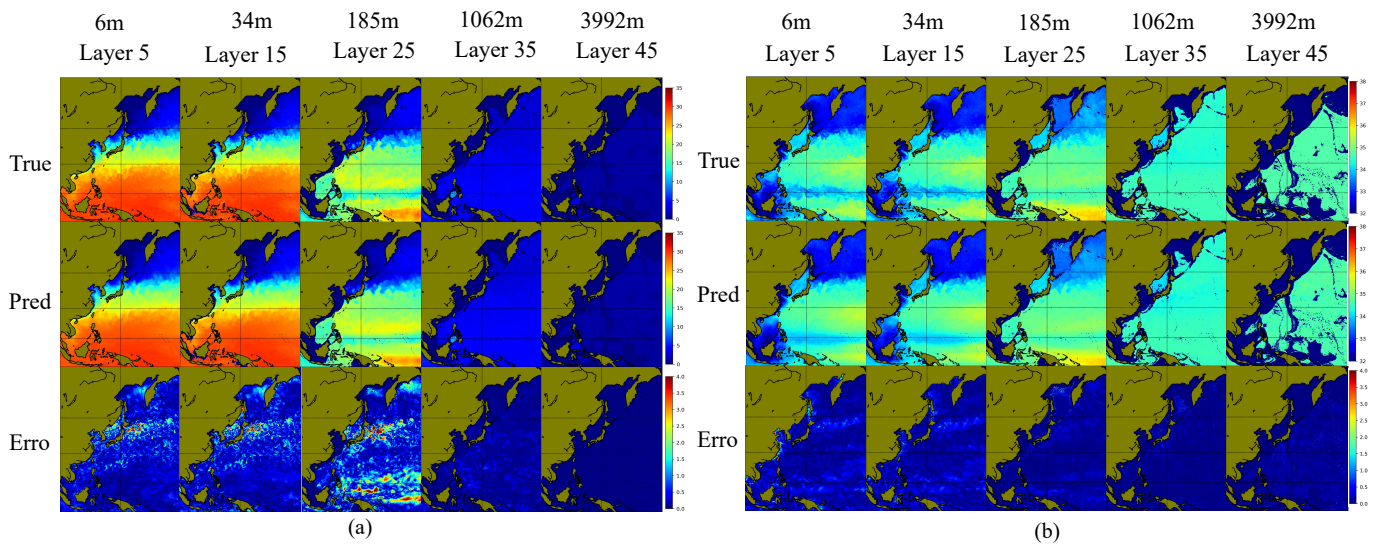


Figure 19. Visualization of the 3D temperature and salinity predictions for day 1 in the Northwest Pacific. (a) Temperature, (b) salinity.

By validating the three-dimensional temperature and salinity models in two sea areas, the growth rate of temperature and salinity errors over 20 days and the characteristics of seasonal error distribution were analyzed. The construction effectiveness of the three-dimensional temperature and salinity forecasting model was confirmed through visualization and analysis of the results.

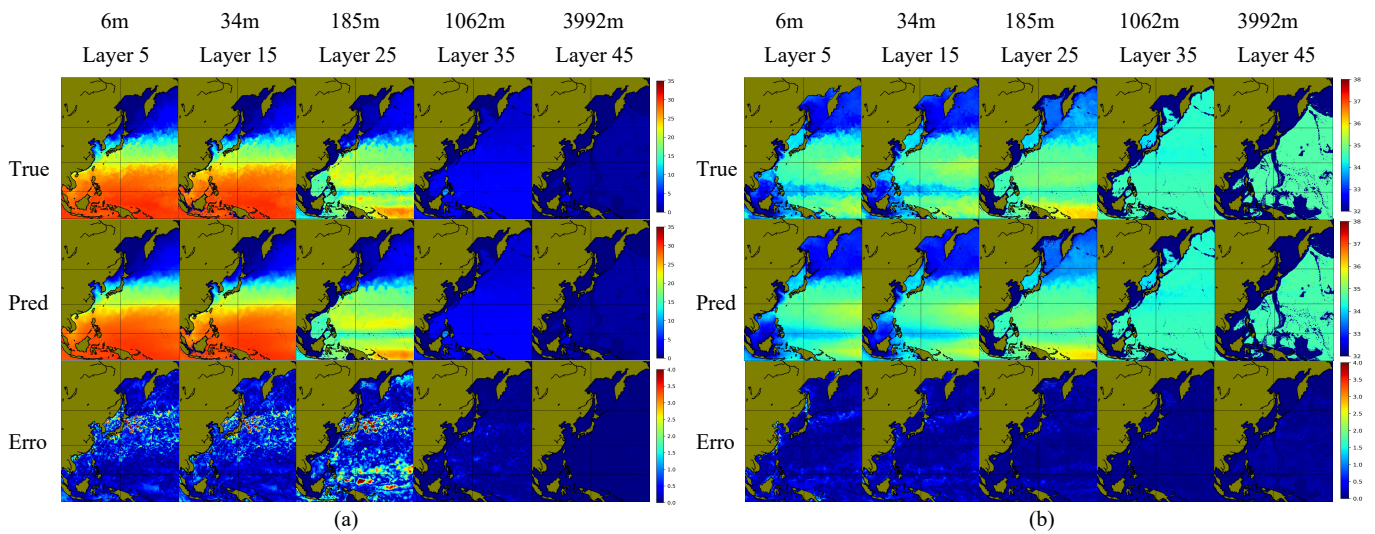


Figure 20. Visualization of the 3D temperature and salinity predictions for day 20 in the Northwest Pacific. (a) Temperature, (b) salinity.

5.4.3. Error Analysis of Prediction

Due to the complex and variable nature of oceanic regions, errors in temperature and salinity predictions are influenced. Thus, we conducted a visual analysis of the prediction errors to explore the impact of dynamic regions on model learning. Taking the Northwest Pacific Ocean as an example, the prediction errors are illustrated in Figure 21, where erro_s represents salinity absolute error, and erro_t represents temperature absolute error. From the figure, it is evident that the errors are primarily concentrated along the Chinese coastline, near the Kuroshio Current, and near the equatorial currents. The coastal region errors are mainly attributed to the irregular shape of the coastline and the variable topography, which complicate the ocean dynamic processes. Additionally, significant tidal effects in these coastal areas make it challenging for the model to accurately capture temperature information distribution [49,50].

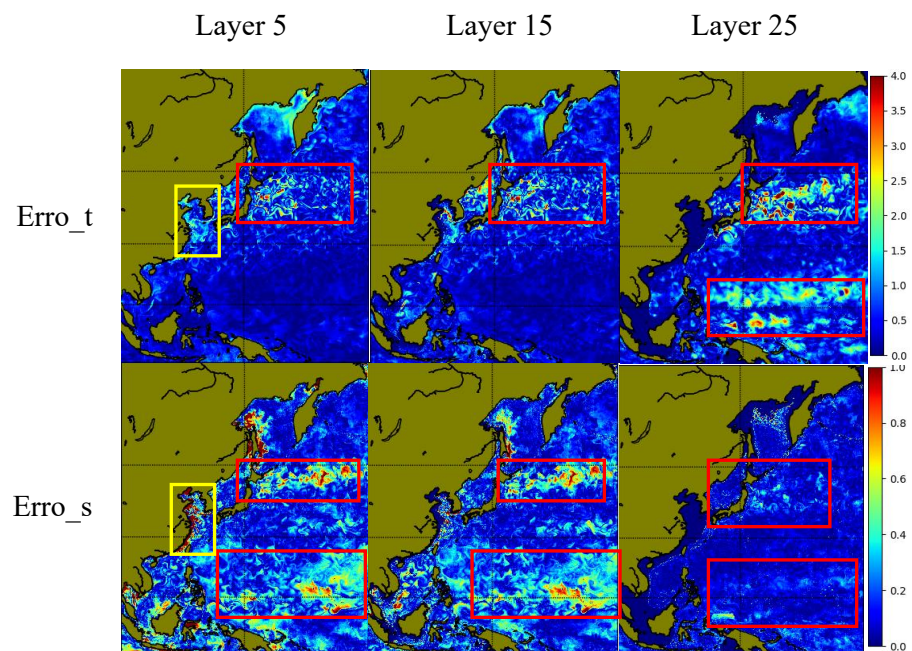


Figure 21. Visualization of temperature and salinity prediction errors. The areas highlighted in the figure are the regions with larger forecast errors in this instance.

In the vicinity of the Kuroshio Current, both temperature and salinity exhibit substantial errors. This phenomenon may be due to the formation of numerous cyclonic and anticyclonic eddies in the Kuroshio Current region. These eddies cause variations in temperature and salinity distribution [51–55], creating interference with the model’s learning process. In the equatorial region, salinity errors are more pronounced, possibly due to the influence of equatorial currents that lead to an imbalance in salinity distribution patterns [56–59]. Temperature, being less affected by equatorial currents, shows errors mainly in the thermocline.

5.4.4. Sensitivity Analysis

Since the predicted SST and SLA serve as intermediate variables for predicting temperature and salinity information as well as sea surface input information, we further analyzed the sensitivity of temperature and salinity predictions to the accuracy of predicted SST and SLA. We designed the following methods for testing, as detailed in Table 11. Specifically, we substituted the true values for predicted values to analyze the impact on temperature and salinity predictions, thus examining how variations in input data affect subsurface temperature and salinity predictions. Method 1 uses true SST and true SLA as model inputs. Method 2 uses true SST and predicted SLA as inputs. Method 3 uses predicted SST and true SLA as inputs. Method 4 uses predicted SST and predicted SLA as inputs.

To demonstrate the feasibility of the validation method, we conducted experimental analysis in the offshore waters of China. The RMSE errors for the 20-day temperature and salinity predictions were plotted as shown in Figures 22 and 23. Figure 22 presents the 20-day temperature forecast results, while Figure 23 displays the RMSE errors for salinity over the 20 days.

Table 11. Table of model sensitivity testing method. The charkmark indicates that this data is selected as the input data.

Inputs	Method 1	Method 2	Method 3	Method 4
SST-True	✓	✓		
SST-Pred		✓	✓	✓
SLA-True	✓		✓	
SLA-Pred				✓

From Figures 22 and 23, it can be analyzed that in the upper ocean (<50 m), SST and SLA have significant impacts on the prediction accuracy of subsurface temperatures. Among these, the accuracy of SST predictions has a major influence. When the SST is predicted more accurately, it reduces the prediction error of the upper ocean temperature. This phenomenon is due to the complex interactions between the upper ocean temperature and the SST through turbulent mixing, dynamic processes, and feedback mechanisms. There is a certain nonlinear mapping relationship between them, which we attempt to learn using deep learning methods. When the SST prediction is inaccurate, the deep learning model’s ability to fit the nonlinear relationship between the ocean surface and subsurface temperatures is impaired, leading to increased temperature prediction errors as SST prediction errors grow.

In the thermocline and halocline regions, the accuracy of SLA predictions significantly affects the error in the entire layer, and it is the dominant factor. The more accurate the SLA, the smaller the errors in temperature and salinity within the layer. This is likely due to the impact of currents, heat and salt transport, and eddies, which bring water with varying temperatures and salinities, affecting the structure of the temperature and salinity layers (reference needed). Accurate SLA predictions help the model capture these dynamic processes, improving the accuracy of temperature and salinity predictions in the layer.

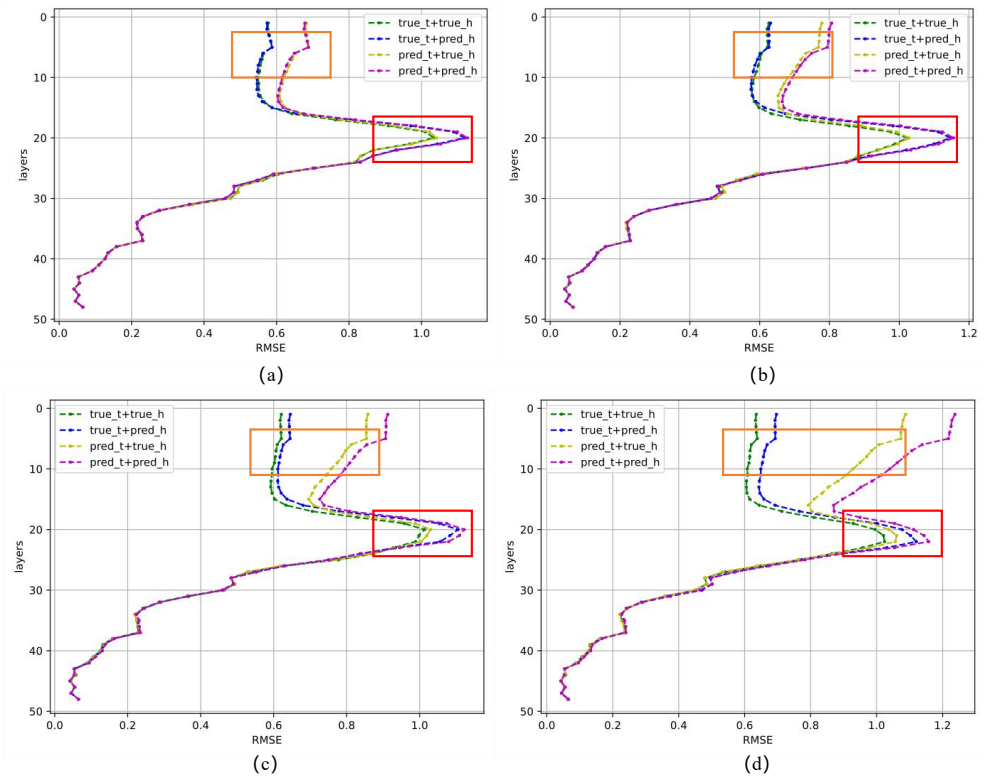


Figure 22. The RMSE curves for temperature with different methods. Figures (a–d) show the errors averaged every 5 days for the 20-day temperature and salinity forecasts. Orange and red box indicate the positions where error changes are noticeably variable over time.

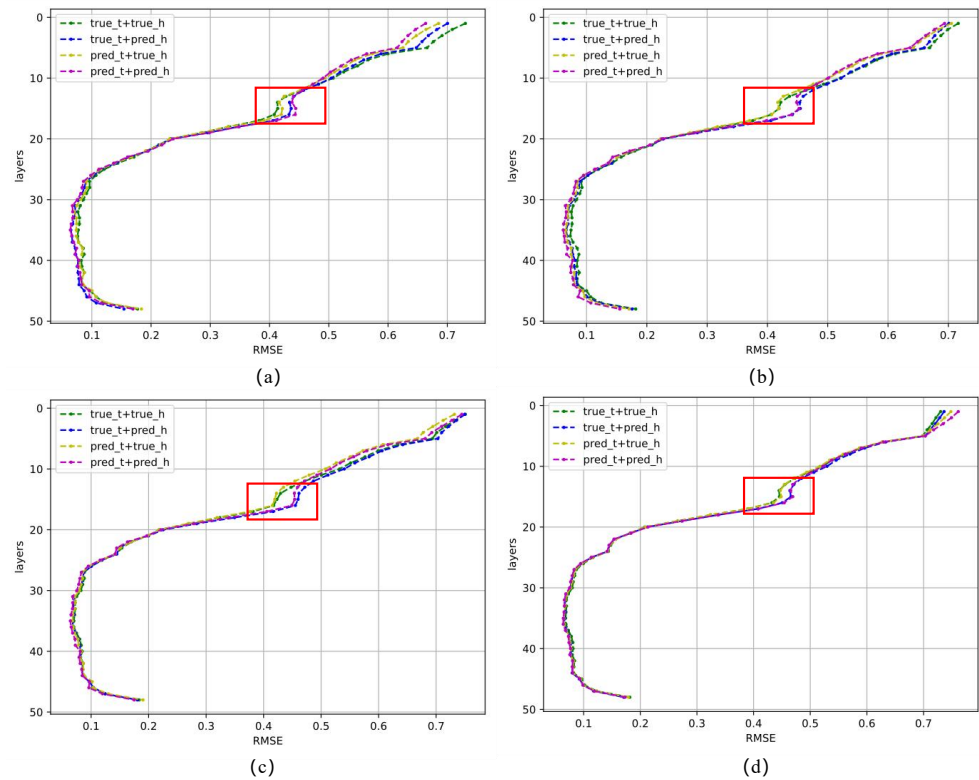


Figure 23. The RMSE curves for salinity with different methods. Figures (a–d) show the errors averaged every 5 days for the 20-day temperature and salinity forecasts. Orange and red box indicate the positions where error changes are noticeably variable over time.

Additionally, from the error plots, it can be seen that when the prediction period exceeds 10 days, the prediction errors for temperature and salinity increase significantly, especially for temperature. This is primarily because the prediction model's accuracy deteriorates for later SST and SLA forecasts, leading to a growing deviation from the true values and a gradual decline in prediction performance.

6. Discussion

This paper utilizes the nonlinear relationship between SST, SLA, and the 3D sea temperature and salinity fields in the subsurface layer to transform the prediction of 3D subsurface temperature and salinity. The approach involves first capturing the horizontal movement of the SST and SLA, and then mapping these to the vertical distribution of subsurface temperature and salinity. The advantage of this method is that it does not require training the model with four-dimensional high-resolution spatiotemporal data, which significantly reduces computational burden and makes the model easier to train. Experimental results demonstrate that this method effectively predicts the 3D temperature and salinity fields of the subsurface ocean for up to 20 days.

To analyze the impact of input data variations on temperature and salinity changes at different depths, we designed sensitivity analysis experiments, substituting true values for predicted values to observe their effects on temperature and salinity predictions. Our analysis revealed that the accuracy of the SST effectively controls changes in the upper ocean temperatures, while the accuracy of the SLA controls the temperature and salinity information in the thermocline. The results of this experiment highlighted the following limitations of our proposed method and further analysis:

(1) Error Accumulation between Prediction and Inversion Models: If there is a bias between the SST and SLA data output by the prediction model and the true data, this bias affects the accuracy of the ocean mixed layer when input into the inversion model. Since the inversion model maps sea surface information to the subsurface temperature and salinity fields using a nonlinear function, greater accuracy in the inversion model leads to more reliable subsurface temperature and salinity information. Improving the performance of both the prediction and inversion models can effectively reduce error accumulation and enhance the accuracy of temperature and salinity predictions.

(2) Information Bias between Satellite Observations and Reanalysis Data: Satellite data, obtained from satellite observations, and reanalysis data, derived from numerical models after assimilation, may have inherent information biases. This bias introduces additional noise, which hampers the deep learning model's ability to learn the mapping from sea surface information to temperature and salinity.

(3) Prediction Errors in Coastal, Estuarine, and High-Current Areas: Prediction errors are notably higher in coastal, estuarine, or high-current regions due to the complexity of terrain and strong current dynamics. Irregular coastlines and variable topography complicate oceanographic processes, affecting accurate predictions of flow and mixing. Additionally, tidal effects in coastal areas significantly impact temperature and salinity distribution, and turbulence and mixing in strong current regions introduce uncertainties in process parameterization, increasing prediction errors.

(4) Duration Limitations: The three-dimensional temperature and salinity prediction method is primarily constrained by the accuracy of SST and SLA forecasts. Sensitivity analysis shows that prediction errors for temperature and salinity in the upper ocean and thermocline increase significantly when the prediction period exceeds 10 days. This limitation is primarily due to the accuracy constraints of SST and SLA predictions.

Based on the issues identified with the current three-dimensional prediction method, future experiments will aim to address these problems by incorporating higher-precision satellite remote sensing data and more advanced deep learning models to further improve the accuracy of three-dimensional temperature and salinity field predictions.

7. Conclusions

This paper employs a method that combines two-dimensional models with multi-source ocean data to effectively predict three-dimensional temperature and salinity fields for 20 days. This approach replaces the previous method of directly constructing prediction models from three-dimensional data. The advantage of this method is that it avoids the challenges associated with stacking high-resolution three-dimensional data over time, which increases the computational resource demands and complicates model training. Analysis of the prediction results shows that this method aligns well with physical principles and accurately predicts most temperatures and salinities. Additionally, by selecting a more advanced deep learning model, we achieved more accurate predictions and conducted a refined analysis of the model's results using various methods.

In summary, we have expanded the understanding of current three-dimensional temperature and salinity prediction methods, offering advancements in data utilization, model architecture, and prediction result analysis.

Author Contributions: Conceptualization, X.C., C.L. and S.Z.; methodology, X.C.; formal analysis, X.C., C.L., S.Z. and F.G.; funding acquisition, C.L. and F.G.; investigation, X.C., C.L., S.Z. and F.G.; resources, C.L., S.Z. and F.G.; software, X.C.; supervision, C.L., S.Z. and F.G.; validation, C.L., S.Z. and F.G.; visualization, X.C.; writing—original draft preparation, X.C.; writing—review and editing, X.C., C.L., S.Z. and F.G. All authors have read and agreed to the published version of the manuscript.

Funding: This research was supported by the Key R&D Program Projects of Heilongjiang Province (NO. 2022ZX01A15), the Cultivation Project of Qingdao Science and Technology Plan Park (No. 23-1-5-yqpy-11-qy).

Institutional Review Board Statement: Not applicable.

Informed Consent Statement: Not applicable.

Data Availability Statement: The daily mean SST data provided by NOAA (<https://www.ncei.noaa.gov/data>, accessed on 10 October 2023) and daily mean SLA data provided by CMEMS (<https://data.marine.copernicus.eu/products>, accessed on 10 October 2023). The high-precision reanalysis data provided by CMEMS (<https://data.marine.copernicus.eu/products>, accessed on 15 October 2023).

Conflicts of Interest: Author Chang Liu was employed by the company Qingdao Hatran Ocean Intelligence Technology Co., Ltd. The remaining authors declare that the research was conducted in the absence of any commercial or financial relationship that could be construed as a potential conflict of interest.

References

1. Tonani, M.; Balmaseda, M.; Bertino, L.; Blockley, E.; Brassington, G.; Davidson, F.; Drillet, Y.; Hogan, P.; Kuragano, T.; Lee, T.; et al. Status and future of global and regional ocean prediction systems. *J. Oper. Oceanogr.* **2015**, *8*, s201–s220. [[CrossRef](#)]
2. Barceló-Llull, B.; Pascual, A.; Mason, E.; Mulet, S. Comparing a multivariate global ocean state estimate with high-resolution in situ data: An anticyclonic intrathermocline eddy near the Canary Islands. *Front. Mar. Sci.* **2018**, *5*, 66. [[CrossRef](#)]
3. Guinehut, S.; Dhomps, A.L.; Larnicol, G.; Le Traon, P.Y. High resolution 3-D temperature and salinity fields derived from in situ and satellite observations. *Ocean Sci.* **2012**, *8*, 845–857. [[CrossRef](#)]
4. Maes, C.; Dewitte, B.; Sudre, J.; Garçon, V.; Varillon, D. Small-scale features of temperature and salinity surface fields in the Coral Sea. *J. Geophys. Res. Ocean.* **2013**, *118*, 5426–5438. [[CrossRef](#)]
5. Edwards, M.; Beaugrand, G.; Hays, G.C.; Koslow, J.A.; Richardson, A.J. Multi-decadal oceanic ecological datasets and their application in marine policy and management. *Trends Ecol. Evol.* **2010**, *25*, 602–610. [[CrossRef](#)] [[PubMed](#)]
6. Fan, W.; Song, J.; Li, S. A numerical study on seasonal variations of the thermocline in the South China Sea based on the ROMS. *Acta Oceanol. Sin.* **2014**, *33*, 56–64. [[CrossRef](#)]
7. Todd, A.; Zanna, L.; Couldrey, M.; Gregory, J.; Wu, Q.; Church, J.A.; Farneti, R.; Navarro-Labastida, R.; Lyu, K.; Saenko, O.; et al. Ocean-only FAFMIP: Understanding regional patterns of ocean heat content and dynamic sea level change. *J. Adv. Model. Earth Syst.* **2020**, *12*, e2019MS002027. [[CrossRef](#)]
8. Morioka, Y.; Taguchi, B.; Behera, S.K. Eastward propagating decadal temperature variability in the South Atlantic and Indian Oceans. *J. Geophys. Res. Ocean.* **2017**, *122*, 5611–5623. [[CrossRef](#)]
9. Zhang, Q.; Wang, H.; Dong, J.; Zhong, G.; Sun, X. Prediction of sea surface temperature using long short-term memory. *IEEE Geosci. Remote Sens. Lett.* **2017**, *14*, 1745–1749. [[CrossRef](#)]

10. Yang, Y.; Dong, J.; Sun, X.; Lima, E.; Mu, Q.; Wang, X. A CFCC-LSTM model for sea surface temperature prediction. *IEEE Geosci. Remote Sens. Lett.* **2017**, *15*, 207–211. [[CrossRef](#)]
11. Qiao, B.; Wu, Z.; Tang, Z.; Wu, G. Sea surface temperature prediction approach based on 3D CNN and LSTM with attention mechanism. In Proceedings of the 2022 24th International Conference on Advanced Communication Technology (ICACT), Pyeongchang, Republic of Korea, 13–16 February 2022; pp. 342–347.
12. Guo, X.; He, J.; Wang, B.; Wu, J. Prediction of sea surface temperature by combining interdimensional and self-attention with neural networks. *Remote Sens.* **2022**, *14*, 4737. [[CrossRef](#)]
13. Liang, S.; Zhao, A.; Qin, M.; Hu, L.; Wu, S.; Du, Z.; Liu, R. A Graph Memory Neural Network for Sea Surface Temperature Prediction. *Remote Sens.* **2023**, *15*, 3539. [[CrossRef](#)]
14. Shao, Q.; Li, W.; Han, G.; Hou, G.; Liu, S.; Gong, Y.; Qu, P. A deep learning model for forecasting sea surface height anomalies and temperatures in the South China Sea. *J. Geophys. Res. Ocean.* **2021**, *126*, e2021JC017515. [[CrossRef](#)]
15. Wei, L.; Guan, L. Seven-day sea surface temperature prediction using a 3DConv-LSTM model. *Front. Mar. Sci.* **2022**, *9*, 905848. [[CrossRef](#)]
16. Hou, S.; Li, W.; Liu, T.; Zhou, S.; Guan, J.; Qin, R.; Wang, Z. MUST: A Multi-source Spatio-Temporal data fusion Model for short-term sea surface temperature prediction. *Ocean Eng.* **2022**, *259*, 111932. [[CrossRef](#)]
17. Hu, S.; Shao, Q.; Li, W.; Han, G.; Zheng, Q.; Wang, R.; Liu, H. Multivariate Sea Surface Prediction in the Bohai Sea Using a Data-Driven Model. *J. Mar. Sci. Eng.* **2023**, *11*, 2096. [[CrossRef](#)]
18. Wu, S.; Zhang, X.; Bao, S.; Dong, W.; Wang, S.; Li, X. Predicting Ocean Temperature in High-Frequency Internal Wave Area with Physics-Guided Deep Learning: A Case Study from the South China Sea. *J. Mar. Sci. Eng.* **2023**, *11*, 1728. [[CrossRef](#)]
19. Zhang, L.; Zhang, Y.; Yin, X. Aquarius sea surface salinity retrieval in coastal regions based on deep neural networks. *Remote Sens. Environ.* **2023**, *284*, 113357. [[CrossRef](#)]
20. Liu, S.; Jia, W.; Zhang, W. DSE-NN: Discretized Spatial Encoding Neural Network for Ocean Temperature and Salinity Interpolation in the North Atlantic. *J. Mar. Sci. Eng.* **2024**, *12*, 1013. [[CrossRef](#)]
21. Xie, H.; Xu, Q.; Cheng, Y.; Yin, X.; Fan, K. Reconstructing three-dimensional salinity field of the South China Sea from satellite observations. *Front. Mar. Sci.* **2023**, *10*, 1168486. [[CrossRef](#)]
22. Wen, Z.; Zhang, H.; Shu, W.; Zhang, L.; Liu, L.; Lu, X.; Zhou, Y.; Ren, J.; Li, S.; Zhang, Q. The SSR Brightness Temperature Increment Model Based on a Deep Neural Network. *Remote Sens.* **2023**, *15*, 4149. [[CrossRef](#)]
23. Tian, T.; Cheng, L.; Wang, G.; Abraham, J.; Wei, W.; Ren, S.; Zhu, J.; Song, J.; Leng, H. Reconstructing ocean subsurface salinity at high resolution using a machine learning approach. *Earth Syst. Sci. Data* **2022**, *14*, 5037–5060. [[CrossRef](#)]
24. Jang, E.; Kim, Y.J.; Im, J.; Park, Y.G.; Sung, T. Global sea surface salinity via the synergistic use of SMAP satellite and HYCOM data based on machine learning. *Remote Sens. Environ.* **2022**, *273*, 112980. [[CrossRef](#)]
25. Jang, E.; Kim, Y.J.; Im, J.; Park, Y.G. Improvement of SMAP sea surface salinity in river-dominated oceans using machine learning approaches. *GISci. Remote Sens.* **2021**, *58*, 138–160. [[CrossRef](#)]
26. Liu, J.; Zhang, T.; Han, G.; Gou, Y. TD-LSTM: Temporal dependence-based LSTM networks for marine temperature prediction. *Sensors* **2018**, *18*, 3797. [[CrossRef](#)] [[PubMed](#)]
27. Zhang, K.; Geng, X.; Yan, X.H. Prediction of 3-D ocean temperature by multilayer convolutional LSTM. *IEEE Geosci. Remote Sens. Lett.* **2020**, *17*, 1303–1307. [[CrossRef](#)]
28. Zuo, X.; Zhou, X.; Guo, D.; Li, S.; Liu, S.; Xu, C. Ocean temperature prediction based on stereo spatial and temporal 4-D convolution model. *IEEE Geosci. Remote Sens. Lett.* **2021**, *19*, 1003405. [[CrossRef](#)]
29. Sun, N.; Zhou, Z.; Li, Q.; Zhou, X. Spatiotemporal prediction of monthly sea subsurface temperature fields using a 3D U-Net-Based model. *Remote Sens.* **2022**, *14*, 4890. [[CrossRef](#)]
30. Muis, S.; Apecechea, M.I.; Dullaart, J.; de Lima Rego, J.; Madsen, K.S.; Su, J.; Yan, K.; Verlaan, M. A high-resolution global dataset of extreme sea levels, tides, and storm surges, including future projections. *Front. Mar. Sci.* **2020**, *7*, 263. [[CrossRef](#)]
31. Banesh, D.; Petersen, M.R.; Ahrens, J.; Turton, T.L.; Samsel, F.; Schoonover, J.; Hamann, B. An image-based framework for ocean feature detection and analysis. *J. Geovisualization Spat. Anal.* **2021**, *5*, 17. [[CrossRef](#)]
32. McWilliams, J.C. The nature and consequences of oceanic eddies. *Geophys. Monogr. Ser.* **2008**, *177*, 5–15.
33. Klemas, V.; Yan, X.H. Subsurface and deeper ocean remote sensing from satellites: An overview and new results. *Prog. Oceanogr.* **2014**, *122*, 1–9. [[CrossRef](#)]
34. Wu, X.; Yan, X.H.; Jo, Y.H.; Liu, W.T. Estimation of subsurface temperature anomaly in the North Atlantic using a self-organizing map neural network. *J. Atmos. Ocean. Technol.* **2012**, *29*, 1675–1688. [[CrossRef](#)]
35. Cazenave, A.; Meyssignac, B.; Ablain, M.; Balmaseda, M.; Bamber, J.; Barletta, V.; Beckley, B.; Benveniste, J.; Berthier, E.; Blazquez, A.; et al. Global sea-level budget 1993–present. *Earth Syst. Sci. Data* **2018**, *10*, 1551–1590.
36. Mao, K.; Liu, C.; Zhang, S.; Gao, F. Reconstructing Ocean Subsurface Temperature and Salinity from Sea Surface Information Based on Dual Path Convolutional Neural Networks. *J. Mar. Sci. Eng.* **2023**, *11*, 1030. [[CrossRef](#)]
37. Zhao, Y.; He, Z.; Jiang, Y. The Inversion of Three-Dimensional Ocean Temperature and Salinity Fields for the Assimilation of Satellite Observations. *J. Mar. Sci. Eng.* **2024**, *12*, 534. [[CrossRef](#)]
38. Xie, H.; Xu, Q.; Cheng, Y.; Yin, X.; Jia, Y. Reconstruction of subsurface temperature field in the south China Sea from satellite observations based on an attention U-net model. *IEEE Trans. Geosci. Remote Sens.* **2022**, *60*, 4209319. [[CrossRef](#)]

39. Zhang, J.; Ning, P.; Zhang, X.; Wang, X.; Zhang, A. Deriving Sea Subsurface Temperature Fields from Satellite Remote Sensing Data Using a Generative Adversarial Network Model. *Earth Space Sci.* **2022**, *10*, e2022EA002804. [[CrossRef](#)]
40. Song, T.; Xu, G.; Yang, K.; Li, X.; Peng, S. Convformer: A Model for Reconstructing Ocean Subsurface Temperature and Salinity Fields Based on Multi-Source Remote Sensing Observations. *Remote Sens.* **2024**, *16*, 2422. [[CrossRef](#)]
41. Ronneberger, O.; Fischer, P.; Brox, T. U-net: Convolutional networks for biomedical image segmentation. In *Medical Image Computing and Computer-Assisted Intervention—MICCAI 2015: 18th International Conference, Munich, Germany, 5–9 October 2015*; Proceedings, Part III 18; Springer: Cham, Switzerland, 2015; pp. 234–241.
42. Gao, Z.; Tan, C.; Wu, L.; Li, S.Z. Simvp: Simpler yet better video prediction. In Proceedings of the IEEE/CVF Conference on Computer Vision and Pattern Recognition, New Orleans, LA, USA, 18–24 June 2022; pp. 3170–3180.
43. Mehta, S.; Rastegari, M. Mobilevit: Light-weight, general-purpose, and mobile-friendly vision transformer. *arXiv* **2021**, arXiv:2110.02178.
44. Aguilar-Martinez, S.; Hsieh, W.W. Forecasts of tropical Pacific sea surface temperatures by neural networks and support vector regression. *Int. J. Oceanogr.* **2009**, *2009*, 167239. [[CrossRef](#)]
45. Arnab, A.; Dehghani, M.; Heigold, G.; Sun, C.; Lučić, M.; Schmid, C. Vivit: A video vision transformer. In Proceedings of the IEEE/CVF International Conference on Computer Vision, Montreal, QC, Canada, 10–17 October 2021; pp. 6836–6846.
46. Li, H.; Qian, J.; Tian, Y.; Rakhlin, A.; Jadbabaie, A. Convex and non-convex optimization under generalized smoothness. *Adv. Neural Inf. Process. Syst.* **2024**, *36*.
47. Jamshidi, S.; Abu Bakar, N. Seasonal variations in temperature, salinity and density in the southern coastal waters of the Caspian Sea. *Oceanology* **2012**, *52*, 380–396. [[CrossRef](#)]
48. Pennington, J.T.; Chavez, F.P. Seasonal fluctuations of temperature, salinity, nitrate, chlorophyll and primary production at station H3/M1 over 1989–1996 in Monterey Bay, California. *Deep Sea Res. Part II Top. Stud. Oceanogr.* **2000**, *47*, 947–973. [[CrossRef](#)]
49. Hu, H.; Wang, J. Modeling effects of tidal and wave mixing on circulation and thermohaline structures in the Bering Sea: Process studies. *J. Geophys. Res. Ocean.* **2010**, *115*. [[CrossRef](#)]
50. Yndestad, H.; Turrell, W.R.; Ozhigin, V. Lunar nodal tide effects on variability of sea level, temperature, and salinity in the Faroe-Shetland Channel and the Barents Sea. *Deep Sea Res. Part I Oceanogr. Res. Pap.* **2008**, *55*, 1201–1217. [[CrossRef](#)]
51. He, Q.; Zhan, H.; Cai, S.; He, Y.; Huang, G.; Zhan, W. A new assessment of mesoscale eddies in the South China Sea: Surface features, three-dimensional structures, and thermohaline transports. *J. Geophys. Res. Ocean.* **2018**, *123*, 4906–4929. [[CrossRef](#)]
52. Sun, W.; An, M.; Liu, J.; Liu, J.; Yang, J.; Tan, W.; Dong, C.; Liu, Y. Comparative analysis of four types of mesoscale eddies in the Kuroshio-Oyashio extension region. *Front. Mar. Sci.* **2022**, *9*, 984244. [[CrossRef](#)]
53. Yao, H.; Ma, C.; Jing, Z.; Zhang, Z. On the Vertical Structure of Mesoscale Eddies in the Kuroshio-Oyashio Extension. *Geophys. Res. Lett.* **2023**, *50*, e2023GL105642. [[CrossRef](#)]
54. Seidov, D.; Mishonov, A.; Reagan, J.; Parsons, R. Eddy-resolving in situ ocean climatologies of temperature and salinity in the Northwest Atlantic Ocean. *J. Geophys. Res. Ocean.* **2019**, *124*, 41–58. [[CrossRef](#)]
55. Liu, S.S.; Sun, L.; Wu, Q.; Yang, Y.J. The responses of cyclonic and anticyclonic eddies to typhoon forcing: The vertical temperature-salinity structure changes associated with the horizontal convergence/divergence. *J. Geophys. Res. Ocean.* **2017**, *122*, 4974–4989. [[CrossRef](#)]
56. Chen, L.; Zhang, R.H.; Gao, C. Effects of temperature and salinity on surface currents in the equatorial Pacific. *J. Geophys. Res. Ocean.* **2022**, *127*, e2021JC018175. [[CrossRef](#)]
57. Vaughan, S.L.; Molinari, R.L. Temperature and salinity variability in the deep western boundary current. *J. Phys. Oceanogr.* **1997**, *27*, 749–761. [[CrossRef](#)]
58. Lynn, R.J. Seasonal variation of temperature and salinity at 10 m in the California Current. *Calif. Coop. Ocean. Fish. Invest. Rep.* **1967**, *11*, 31.
59. Johnson, G.C.; McPhaden, M.J.; Rowe, G.D.; McTaggart, K.E. Upper equatorial Pacific Ocean current and salinity variability during the 1996–1998 El Niño–La Niña cycle. *J. Geophys. Res. Ocean.* **2000**, *105*, 1037–1053. [[CrossRef](#)]

Disclaimer/Publisher’s Note: The statements, opinions and data contained in all publications are solely those of the individual author(s) and contributor(s) and not of MDPI and/or the editor(s). MDPI and/or the editor(s) disclaim responsibility for any injury to people or property resulting from any ideas, methods, instructions or products referred to in the content.